UNIVERSITY OF CALIFORNIA SAN DIEGO

Patterning and Validation Technique for Arbitrary Anisotropic Impedance Surfaces

A Dissertation submitted in partial satisfaction of the
requirements for the degree
Doctor of Philosophy

in

Electrical Engineering (Electronic Circuits and Systems)

by

Jiyeon Lee

Committee in charge:

Professor Daniel F. Sievenpiper, Chair
Professor Gert Cauwenberghs
Professor Eric E. Fullerton
Professor Boubacar Kante
Professor Vitaliy Lomakin

2018

The Dissertation of Jiyeon Lee is approved, and it is acceptable in quality and form for publication on microfilm and electronically:

_____

_____

_____

_____

_____

Chair

University of California San Diego

2018

DEDICATION

To my family and three cats, and all of my dearest friends

EPIGRAPH

You are never too old to set another goal or to dream a new dream.

— C. S. Lewis

TABLE OF CONTENTS

LIST OF FIGURES

ACKNOWLEDGEMENTS

Foremost, I would like to thank my advisor, Prof. Daniel Sievenpiper, for his continuous support, patience and guidance throughout the entirety of my Ph.D program. I feel lucky that I have worked on the AFOSR project in his group, which is a great research project and gives me lots of inspirations so that I could develop my creativity and strength in electromagnetics and metamaterial field. I would like to thank again to Prof. Sievenpiper for encouraging me to keep up the good work and trusting me with the project. He is the best advisor who always provides insightful discussion, and the open-minded mentor taking care of students.

I would like to express the greatest appreciation and thanks to my undergrad advisors, Prof. Dongwook Park, Prof. Youngmin Kim and Prof. Hosung Choo for their endless support and love. I've been very lucky to have lifetime mentors who always give the best advice not only for academic research but also for my life. I could not have started this journey without their encouragement which inspired me to realize my potential as a research scientist.

I would especially like to thank Prof. Bang-Sup Song for his support and encouragement. It was my honor to have his advice and immense knowledge and many insightful discussions and suggestions. It would have been impossible to finish my degree at UCSD without his support. I would also like to thank my committee members, Prof. Boubacar Kante, Prof. Eric Fullerton, Prof. Gert Cauwenberghs, and Prof. Vitaliy Lomakin for taking the time to be part of my committee and for their comments and suggestions.

There was a tremendous help from my lab mates at the Applied Electromagnetics Group, which helped me get through tough time at UCSD and made me successfully finish this journey. I would especially like to thank Sanghoon Kim for his amazing contribution to

our lab and being a great senior to us. I am also deeply thankful to my friends especially from Prof. Rebeiz's group and Prof. Mercier's group for their huge help and friendship.

Lastly, my most sincere gratitude goes out to my family and friends in Korea. Words can not express how grateful I am to them and this Ph.D degree would not have had a meaning for me without them. I dedicate this thesis to my family and friends. I thank my lovely younger sister Jeehee for taking care of parents and three cats well while I have been away from home. Also, I deeply thank my parents who always believed in me and gave great supports and unconditional love. A special thank to my old friends (too many to list here but you know who you are!) for endless support and true friendship for a long time. I especially thank Leang's family in Malaysia for continuous support and friendship.

To my dear friend Seungjune Lee - I could not have survived from this long journey without your encouragement. Finally the long-awaited day has come, and I believe you are happily watching all these from heaven.

The material in this dissertation is based on the following papers which are either published or preparation for publication.

Chapter 2 is based on and is mostly a reprint of the following paper: **J. Lee**, D. Sievenpiper, "Patterning Technique for Generating Arbitrary Anisotropic Impedance Surfaces", *IEEE Transactions on Antennas and Propagation*, vol. **64**, no. 11, pp. 4725-4732, December 2016. The dissertation author was the primary author of this material.

Chapter 3, in part, are currently being prepared for submission for publication of the material as it may appear in: **J. Lee**, D. Sievenpiper, Design of Arbitrary Anisotropic Impedance Surface for Reducing Leakage of Surface Wave. The dissertation author was the primary author of this material.

Chapter 4 is based on and is mostly a reprint of the following paper: **J. Lee**, D. Sieven-

piper, Extracting Surface Impedance Method for an Anisotropic Polygon Unit Cell,*IEEE Antennas and Propagation Symposium*, San Diego, CA, July 9, 2017; **J. Lee**, D. Sievenpiper, "Method for Extracting the Effective Tensor Surface Impedance Function from Nonuniform, Anisotropic, Conductive Patterns", *IEEE Transactions on Antennas and Propagation*, Submitted. The dissertation author was the primary author of this material.

Jiyeon Lee

La Jolla, CA

November 2018

VITA

2006	B. S. in Electrical and Electronics Engineering, Hongik University, Seoul, Korea
2008-2011	Software Engineer, SK C&C, Seoul, Korea
2013	M. S. in Electrical Engineering (Electronic Circuits and Systems), University of California San Diego, USA
2013-2018	Graduate Student Researcher, University of California San Diego, USA
2018	Ph. D. in Electrical Engineering (Electronic Circuits and Systems), University of California San Diego, USA

PUBLICATIONS

Journal Articles

J. Lee, D. Sievenpiper, "Design of Arbitrary Anisotropic Impedance Surface for Reducing Leakage of Surface Wave", in preparation.

J. Lee, D. Sievenpiper, "Method for Extracting the Effective Tensor Surface Impedance Function from Nonuniform, Anisotropic, Conductive Patterns", IEEE Transactions on Antennas and Propagation, submitted

J. Lee, D. Sievenpiper, "Patterning Technique for Generating Arbitrary Anisotropic Impedance Surfaces", IEEE Transactions on Antennas and Propagation, vol. 64, no. 11, pp. 4725-4732, December 2016

Y. Zhai, **J. Lee**, Q. Hoang, D. Sievenpiper, H. Garudadri, T. Ng, Printed Wireless Fluidic Pressure Sensor, Flexible and Printed Electronics, accepted for publication.

H. Wakatsuchi, J. J. Rushton, **J. Lee**, F. Gao, M. Jacob, S. Kim, D. F. Sievenpiper, Experimental Demonstration of Nonlinear Waveform-Dependent Metasurface Absorber with Pulsed Signals, Electronics Letters, vol. 49, no. 24, pp. 1530-1531, November 2013

Conference Papers

J. Lee, D. Sievenpiper, Extracting Surface Impedance Method for an Anisotropic Polygon Unit Cell, 2017 IEEE Antennas and Propagation Symposium, San Diego, CA, July 9, 2017

A. Li, E. Forati, S. Kim, **J. Lee**, Y. Li, D. Sievenpiper, Periodic Structures for Scalable High-Power Microwave Transimitters, 2017 IEEE Antennas and Propagation Symposium, San Diego, CA, July 9, 2017

D. Sievenpiper, S. Kim, J. Long, **J. Lee**, Advances in Nonlinear, Active, and Anisotropic Artificial Impedance Surfaces, 2016 European Microwave Conference, London, United Kingdom, October 6, 2016

D. Sievenpiper, R. Quarfoth, **J. Lee**, "Advances in Anisotropic Artificial Impedance Surfaces", 9th International Congress on Advanced Electromagnetic Materials in Microwaves and Optics, Oxford, United Kingdom, September 7-12, 2015

ABSTRACT OF THE DISSERTATION

Patterning and Validation Technique for Arbitrary Anisotropic Impedance Surfaces

by

Jiyeon Lee

Doctor of Philosophy in Electrical Engineering (Electronic Circuits and Systems)

University of California San Diego 2018

Professor Daniel F. Sievenpiper, Chair

Anisotropic impedance surfaces have been demonstrated to be useful for a variety of applications ranging from antennas, to surface wave guiding, to control of scattering. To increase their anisotropy requires elongated unit cells which have reduced symmetry and thus are not easily arranged into arbitrary patterns.

We'll discuss the limitations of existing patterning techniques and explore options for generating anisotropic impedance surfaces with arbitrary spatial variation. A new patterning technique, called a point-shifting method combined with a Voronoi cell generation technique, will be introduced that allows a wide range of anisotropic impedance profiles. This approach

can be used to produce patterns which include highly elongated cells with varying orientation, and cells which can smoothly transition between square, rectangular, hexagonal, and other shapes with a wide range of aspect ratios. Various applications fabricated by point sifting method will be introduced. Also, we'll discuss a new method to extract surface impedances from arbitrarily shaped patch cells using the moment of inertia equations for validating designed surface impedances. We verify the method by comparing the results between PEC patterns and impedance boundary sheets to which the extracted impedances are applied. Simulations of the patterns are verified by measurements as well. Lastly, a relationship between tensor impedances and a geometry function of impedance pattern which is called a starting function has been explored. We'll discuss about inverse gradient procedure and its condition, which is used to find a correlation between tensor impedances and a starting function.

Chapter 1

Introduction

1.1 Motivations for Anisotropic Impedance Surfaces

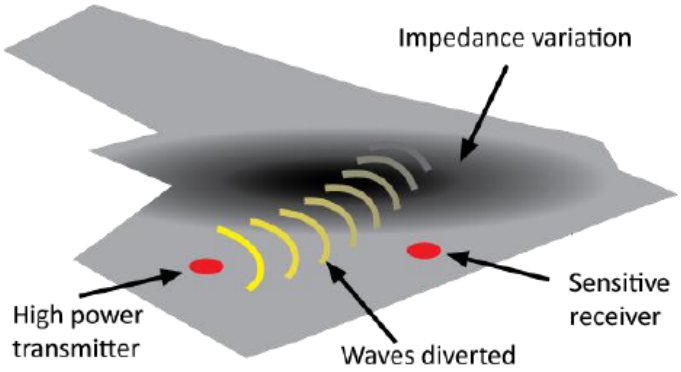

Figure 1.1: Control of the aircrafts interaction with the electromagnetic spectrum

An artificial impedance surface is a metasurface which is fabricated with periodic metallic patches on a grounded dielectric substrate. It has been used for various applications including control of surface waves [1, 2], scattering [3], conformal antennas [4] and waveguides [5, 6, 7]. Fig. 1.1 shows that electromagnetic waves are the primary medium for both communicating with and sensing of aircraft. Thus control of the aircrafts interaction with the electromagnetic spectrum is critically important.

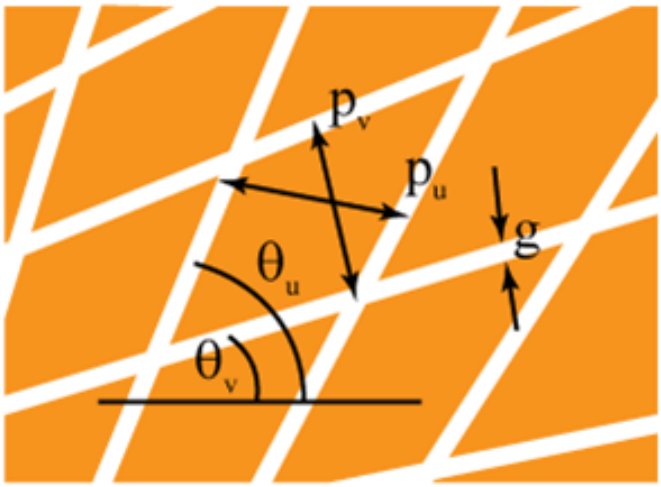

Figure 1.2: Anisotropic impedance surfaces designed as a lattice of metal patches. The property of anisotropic impedance surfaces are determined by the shape and size of unit cell, gaps between patches, and so on.

The artificial impedance surface allows us to control the interaction between electromagnetic waves and metal or composite surfaces. Their electromagnetic properties are defined by the thickness of the substrate, and the capacitance between patches, which together determine the effective surface impedance. Varying the cell size and shape allows the impedance to be controlled. Vertical conducting vias are sometimes also used, but they are only necessary if very high impedance values are needed, or to completely block surface waves [8]. Initial impedance surfaces consisted of simple square or hexagonal cells. However, reducing the symmetry of the cells allows the surface to have anisotropic impedance properties. This is important for applications such as surface wave cloaking, interference reduction between RF apertures, control over polarization, and conversion between transverse magnetic (TM) and transverse electric (TE) surface waves.

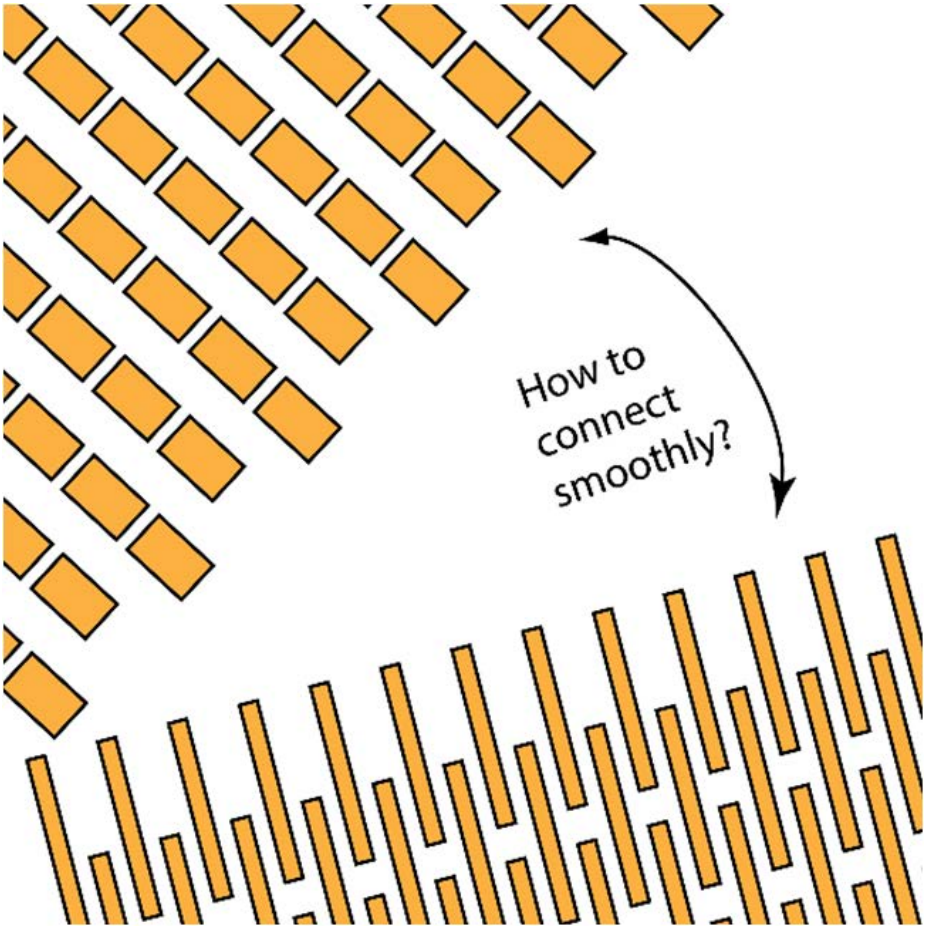

Figure 1.3: Motivations for Anisotropic Impedance Surfaces. A primary challenge in current artificial impedance surface research is how to pattern impedance surfaces to produce arbitrary impedance profiles when the surface is highly anisotropic or has impedance that varies dramatically with position.

1.2 Patterning and Validation Technique

Until recently it was not possible to create smoothly varying, highly anisotropic impedance functions because of the difficulty of patterning regions in which the cell size, shape and orientation varied. Illustrated in Fig. 1.3, there was no available method to smoothly connect these regions with different impedance values and with different primary directions, aside from drawing each cell manually, which is impractical. In attempting to produce surfaces with a high degree of anisotropy, we have become limited in the range of impedance profiles that we can produce. We would like to print arbitrary patterns, but we face the challenge of how to transition between regions of different impedance.The challenge is how to pattern elongated unit cells which allow high anisotropy, but to also create arbitrary and smoothly varying impedance patterns. All previous work in this area used discrete regions of different impedance values or directions [3, 5].

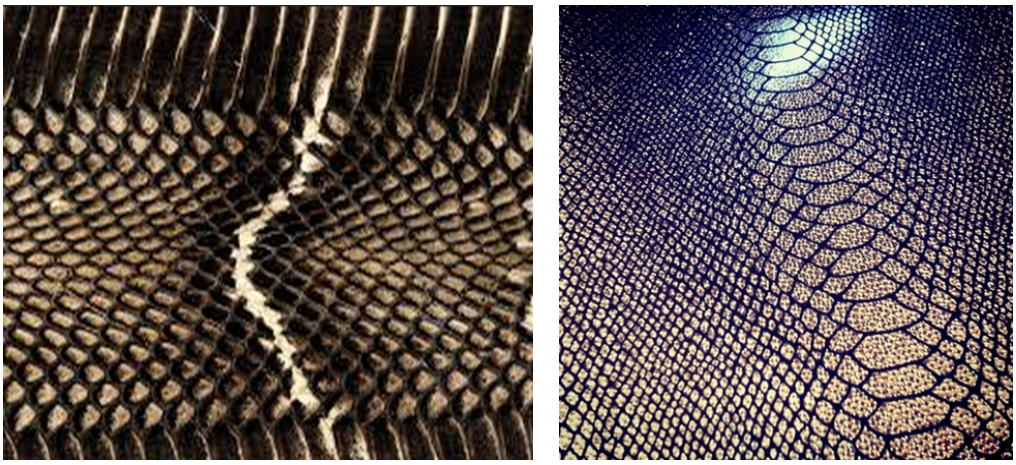

Figure 1.4: Snake skin. As the shape and size of cells change, they fit in smoothly.

In general, these surfaces will consist of smoothly varying impedance profiles, so we need to develop a patterning technique that enables the shape and orientation of the patches, and the electromagnetic impedance associated with them, to vary smoothly and continuously across a two-dimensional surface like a snake skin shown in Fig. 1.4.

Fig. 1.5 is an example of anisotropic impedance surface, shown in cartoon only. This surface is made by simply stretching the surface in different ways to warp the unit cells. We presently do not have a way to pattern such structures to produce smoothly varying impedance functions. In this example, if the surface were extended over a large distance and a similarly warping method is applied, the cells near the edges would become too large or too small, similar to the problem with conformal mapping.

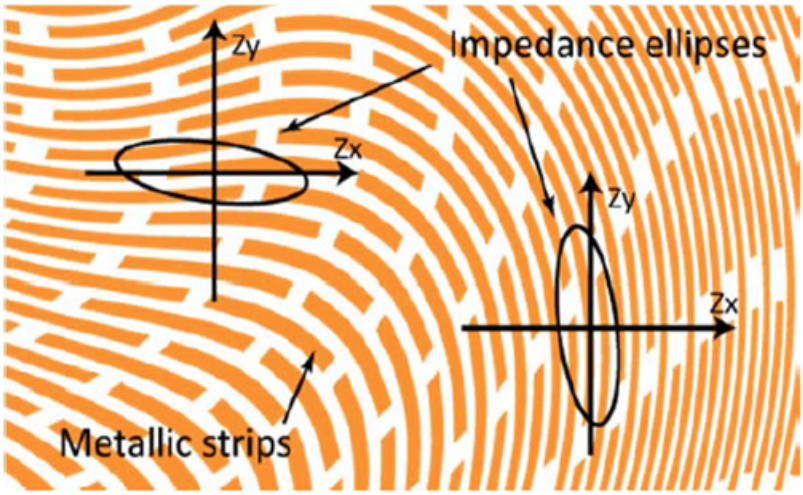

Figure 1.5: Manually designed anisotropic impedance surface

1.3 Summary of Dissertation

This dissertation presents the procedure of designing arbitrary anisotropic impedance surfaces and details of each step as shown in Fig. 1.6.

Chapter 2 introduces a new patterning technique, the point-shifting method which allows us to generate smoothly varying arbitrary anisotropic impedance surfaces.

Chapter 3 presents a design of smoothly varying impedance surface to block the surface wave for shielding purpose. The surface wave shielding pattern is discussed and simulation results are included. The pattern can be used to prevent or reduce the leakage of

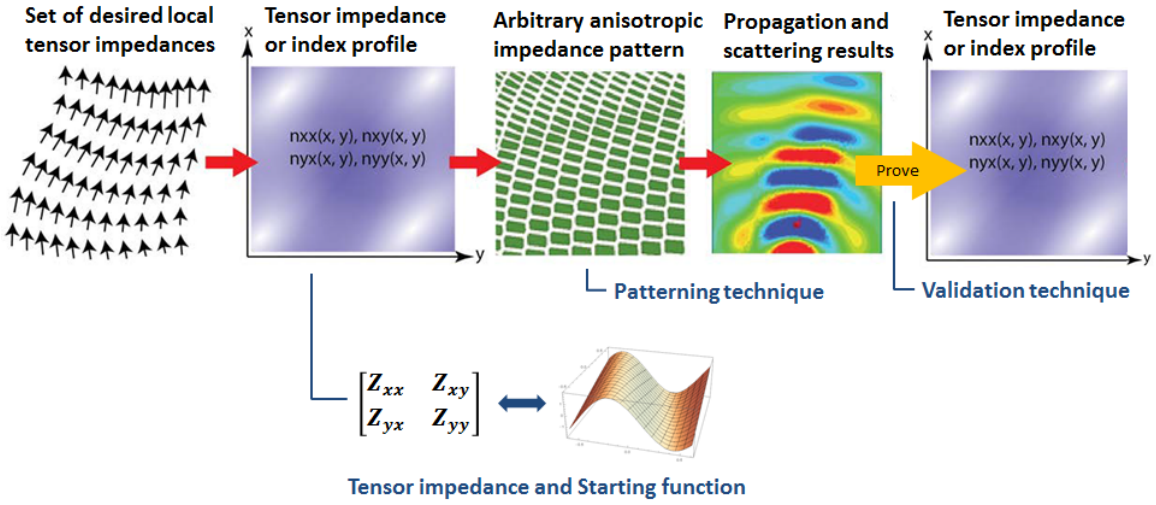

Figure 1.6: The flow of designing impedance surface. It starts from a desired current profile including a patterning step and a validation step.

the surface waves from a slot or a crack on the plane.

Chapter 4 addresses a validation technique to extract the effective tensor surface impedance function from nonuniform, anisotropic, conductive Patterns. The method enable to find tensor surface impedances for asymmetric and polygon unit cells which are not possible to be analyzed in periodic boundaries.

Chapter 5 studies a relationship between a starting function and tensor impedance function. As the tensor impedance function meeting the condition of inverse gradient is found, we can design a pattern based on the tensor impedance in a certain condition.

Chapter 2

Patterning technique for generating smooth anisotropic impedance surfaces

2.1 Limitation of conventional anisotropic impedance surface

Several existing approaches to patterning anisotropic surfaces can be found in the literature, and examples are shown in Fig. 2.1. The first anisotropic impedance surface [9] shown in Fig. 2.1(a) used slices in a lattice of square patches, that are rotated to an arbitrary angle. For example, if the slices are oriented along the Y direction, the structure has twice as many capacitive gaps along X as along Y, due to the extra capacitance of the slice. Thus, the maximum anisotropy of such a structure is roughly 2:1. A structure based on circular patches [10] shown in Fig. 2.1(b) is similar and suffers from the same limitation. In Fig. 2.1(c) the structure [11] involved capacitive regions connected by inductive bars that are rotated to arbitrary angles. If the angle of rotation varies too rapidly between adjacent cells,

the capacitive regions do not line up. It is also limited by the use of a square grid. Fig. 2.1(d)

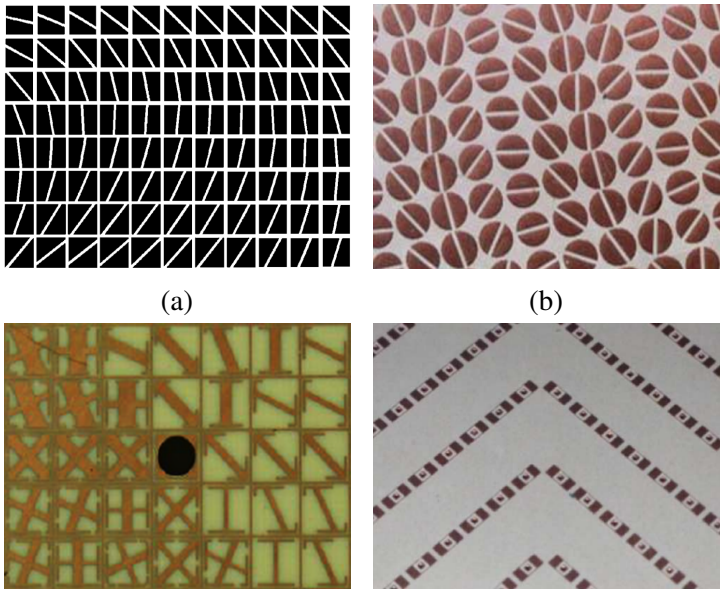

Figure 2.1: Conventional Impedance Surfaces. Examples of anisotropic surfaces include (a) square (IEEE copyright line © 2010) or (b) circular patches with slices rotated to an arbitrary angle, (IEEE copyright line © 2015) or (c) other patterns confined to a square lattice, (IEEE copyright line © 2015) as well as (d) lower symmetry cells that cannot be arranged into arbitrary patterns (IEEE copyright line © 2014).

shows that elongated unit cells [3] can provide a high range of anisotropy however these require a rectangular grid. Any design that reduces symmetry of the lattice itself cannot be patterned to include an arbitrarily varying angle of anisotropy.

Other approaches exist for creating smoothly varying and arbitrary geometrical patterns, however they dont have the required properties for artificial impedance surfaces. Conformal mapping [12, 13], illustrated in Fig. 2.2(a) is one option which is commonly used for defining effective permeability or permittivity in transformation optics applications [14]. It could potentially be applied to generating cells for impedance surfaces. However, it has the limitation that the cell size, shape, and orientation would be highly dependent on the divergence of the local impedance function. As illustrated in Fig. 2.2(a), as the lines

diverge, the cells get larger in the direction perpendicular to the lines, which also sets their

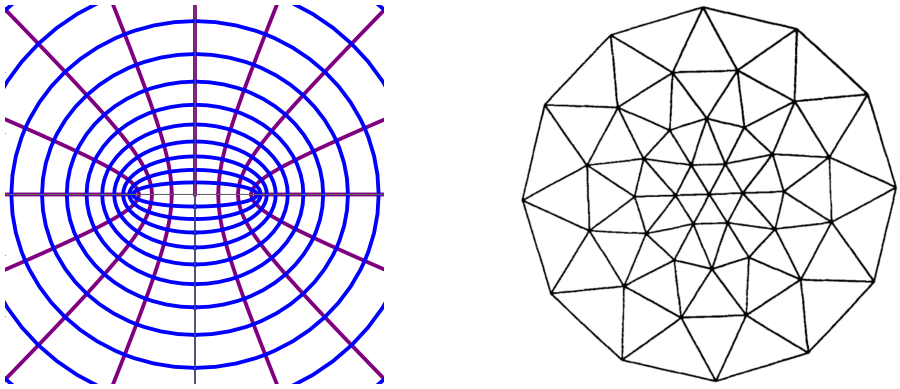

(a) (b)

Figure 2.2: Other possible approaches to patterning smoothly varying impedance surfaces include (a) conformal mapping, and (b) mesh generation techniques. Neither of these produce anisotropic impedance surfaces with the properties needed for applications.

orientation. This is true of any patterning technique that relies on defining cell boundaries by continuous lines. Thus, while conformal mapping is useful for determining impedance profiles to achieve certain functional properties, it is not appropriate for defining the unit cells to create those impedance profiles. Our approach to be described below provides more freedom in defining impedance surfaces that have dramatic changes in impedance over short distances.

Mesh generation techniques have been developed for physical modeling codes for many years, and typically produce patterns such as shown in Fig. 2.2(b) [15]. These could potentially be applied to patterning impedance surfaces as well. However, they are generally designed to provide a specific average cell density, without concern for the details of the cell shape. For impedance surfaces the cell shape is very important for determining the anisotropic impedance values.

We explored another option that we called the point density method as illustrated in Fig. 2.3. The idea is to start with a function in Fig. 2.3(a), the slope of which represents

the local impedance. By traversing that function, we can define a point which represents

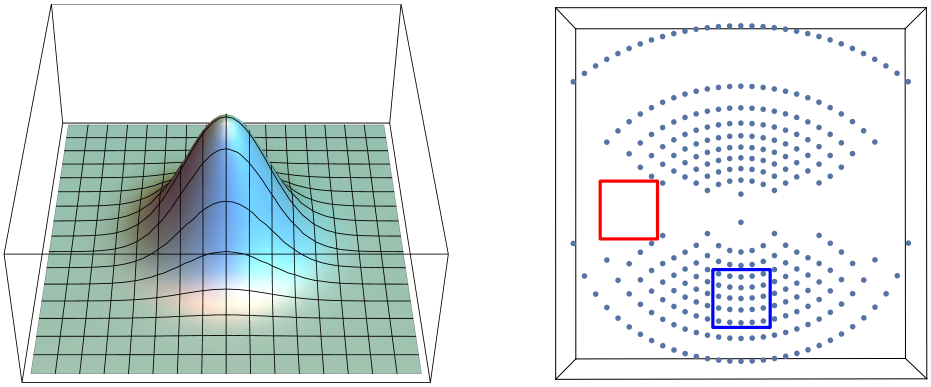

(a) (b)

Figure 2.3: Point density approach. Another method called the point density approach involves choosing points with a density based on (a) a function whose slope represents the local impedance function. The resulting set of points (b) represents the centers of the cells, but their location depends on the path over which one traverses the original function. Discrepancies are indicated at the red and blue squares.

the center of a unit cell each time the function reaches an integer value, or at some other uniform interval of z-axis and another axis among x and y axis. The problem with this approach is that it is highly dependent on the path over which one traverses the function. As shown in Fig. 2.3(b) it does not produce a unique set of unit cells. This is one example of many path-dependent approaches that we determined were unable to produce patterns which required properties for impedance surfaces.

2.2 Patterning Technique - Point Shifting Method

2.2.1 Dot patterning

We developed a patterning technique to produce arbitrary anisotropic surfaces which we call the point shifting method. For our patterning method, we define a function that is

related to the desired surface impedance in each direction, which is related to the cell size in that direction. We currently choose this starting function based on knowledge of the desired

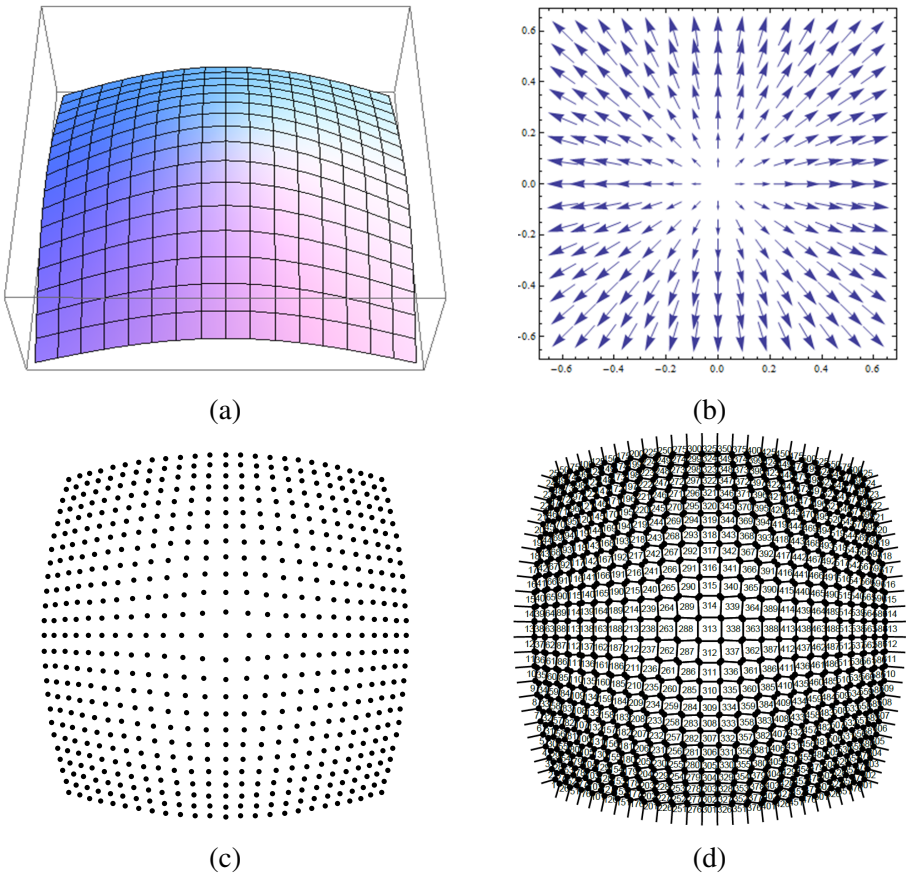

Figure 2.4: Procedure of point shifting method. (a) A starting function with a local maximum. (b) A set of gradient vectors which define the movement of points. (c) The final set of points. (d) The unit cells generated by the Voronoi method.

cell profile. We then define a uniform grid of points with a period equal to the average cell size. Next, we shift each point in proportion to the gradient vector of the starting function. This is illustrated in Fig. 2.4(a) which shows a function with a local maximum, and in Fig. 2.4(b) which shows each point moving with a direction and magnitude that is in proportion to its gradient vector. The result is that the distance between neighboring points is expanded near local maxima, and compressed near local minima. In regions with constant slope, the points all shift by the same amount, resulting in no change in the distance between them.

Fig. 2.4(c) shows the final lattice of points for this example. Anisotropic cells are created by compressing or stretching the distance between points in one direction relative to the other. Thus, the anisotropy in the final lattice of points is defined by the anisotropy of the curvature in the starting function. The cells are generated from the grid of points using a Voronoi technique, as shown in Fig. 2.4(d).

2.2.2 Voronoi function

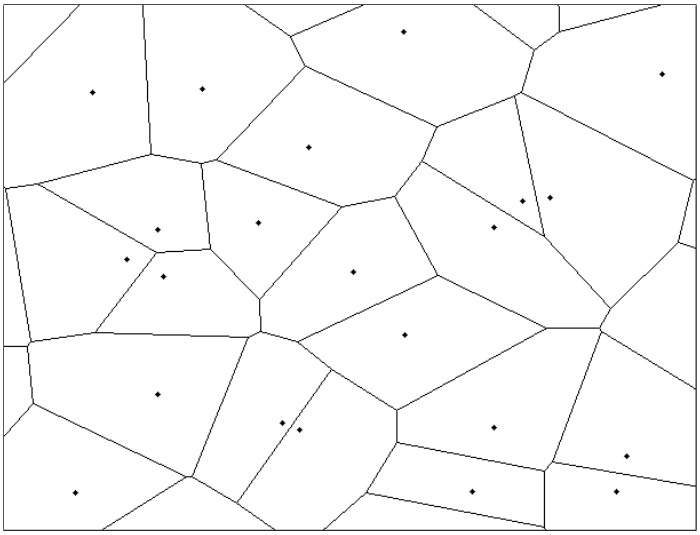

Figure 2.5: Voronoi diagram for a random set of points. Each cell is defined as the region that is closer to each point than to any of its neighbors.

A Voronoi diagram is an approach for dividing regions based on a set of points and the Euclidean distance between those points [16]. To create a two-dimensional Voronoi diagram, one draws a midline between each pair of neighboring points, which is perpendicular to a line drawn from one point to the other. For each point, the collection of midlines to each of its neighbors defines the cell associated with that point. This is the same method used to define Brillouin zones for crystals [17] Fig. 2.5 shows an example Voronoi diagram for a random set of points. The Voronoi function is available in codes such as Mathematica and

MATLAB.

The relationship between the properties of the Voronoi cells and the surface impedance is defined by the details of the cell geometry. For a fixed substrate thickness and dielectric constant, higher impedance can be obtained using larger cells, or smaller gaps [1]. The surface impedance is defined as the ratio of the tangential electric and magnetic fields. It can be direction-dependent in the case of anisotropic surfaces, and the impedance along a particular direction is primarily determined by the length and gap width in that direction [5]. Varying only the gap width limits the range of available impedance values, but allowing the cell size to vary provides a wider design space. Furthermore, more complex anisotropic structures cannot be designed without either elongated unit cells (which cannot be patterned into arbitrary functions with any existing techniques) or more complicated cell geometries [11]. For this reason we are developing a patterning technique that allows for continuous variation of cell size, shape, and orientation.

We note that polygon unit cells in the patterns are generated by Voronoi function so that their shapes are limited. The shape of unit cell is determined by how many we have nearest neighbor dots and how far they are spread out. We could have 8, 10 or other more sides when we warp these but if the surface is smoothly varying, we are not going to have any points where we end up with the force coming in one way and out the other way. Everything is going to approximate some kind of largely convex multi-side object that will be somewhere between rectangle or hexagon or minor variation of those. And its only few special cases can produce more than 6 sides, and even getting into 8 sides requires some settled points.

2.2.3 Gap generation

After an array of cells is patterned on the XY plane, a gap is required between neighboring cells to define an artificial impedance surface. The process of generating a constant gap width starts with calculating the distance between the center point and one side of the cell. Each cell is defined by its center point and vertices. We define a line connecting each pair of vertices, as shown in Fig. 2.6(a), and then calculate the length of the segment running from the center point and perpendicular to this line, as shown in Fig. 2.6(b). The next step is calculating the ratio between the distance calculated in Fig. 2.6(b) and half of the assigned gap which is shown in Fig. 2.6(c) as a blue line. After the ratio is obtained, it can be used to calculate the coordinates of new vertexes for each cell. Each vertex is moved toward the center of the cell by a distance that is defined by the ratio calculated above, as shown in Fig. 2.6(d). This process is used to create each new side of the cell, as shown in Fig. 2.6(e). However the varying angles between sides create errors in the definition of the new cell which must be corrected. The solution is to take the intersections of lines created from the new sides to generate corrected vertices, shown as blue dots in Fig. 2.6(f). These new points complete the new cell with a constant gap width. This process is repeated for all cells in the array to generate a file which defines the metallic pattern that forms the artificial impedance surface.

2.2.4 Advantage of Point Shifting Method

The cells are generally designed to be electrically small at the frequency of interest so that they can be considered in the effective medium limit, and the surface can be described as an effective impedance boundary. Refraction or reflection [1] does not occur at the individual cell boundaries, but rather due to large-scale variation in the effective surface

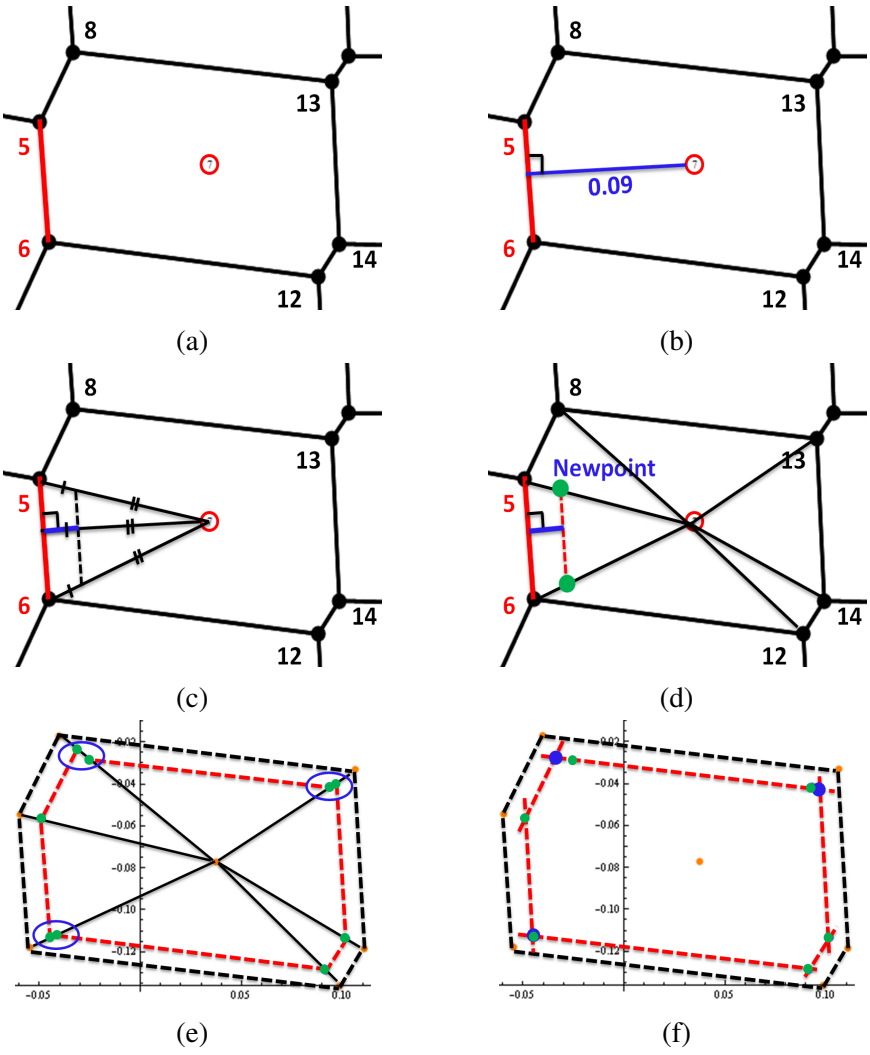

Figure 2.6: Process of generating a constant gap. (a) A cell defined by a center point and vertices. (b) A segment shown in blue from the center point to a line connecting two vertices shown in red. (c) Half the intended gap width is shown in blue. (d) Vertices are moved toward the center point by a distance that is proportional to the gap width. (e) Errors are introduced due to the varying angles between adjacent sides. (f) The errors are corrected by placing new vertices at the intersections between lines defined by each side. The final cell has constant gap width.

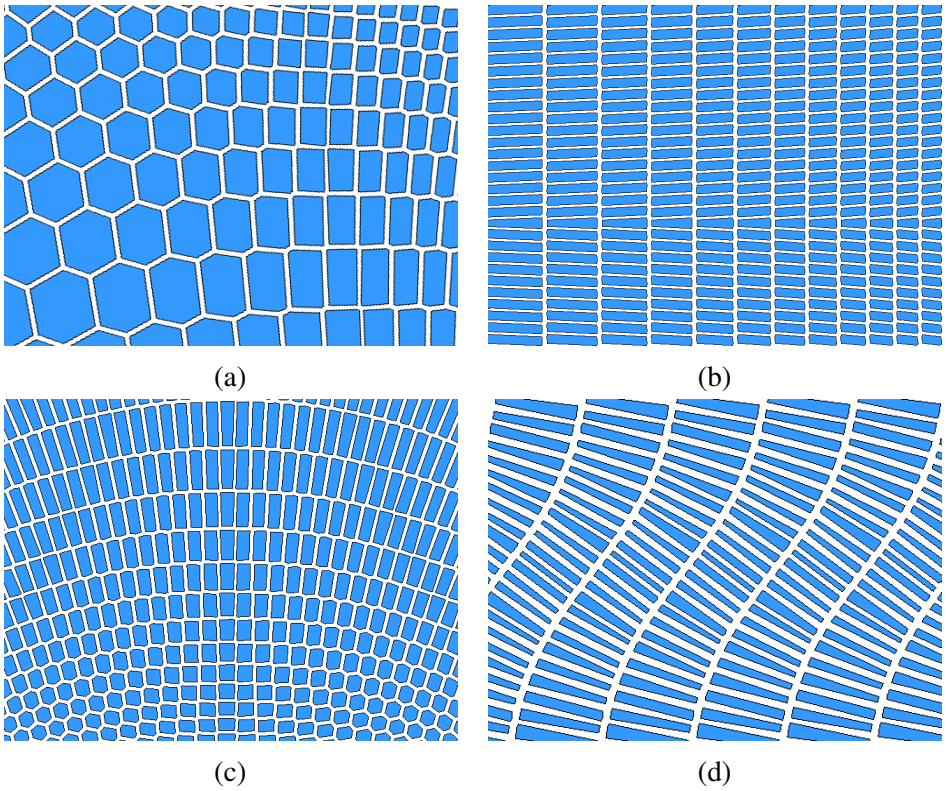

Figure 2.7: Examples of various patterns that can be produced by this technique. (a) Varying cell shape. (b) Gradient of impedance. (c) Varying orientation. (d) Extreme variation with high anisotropy.

impedance.

Fig. 2.7 shows the range of properties that can be created using our point shifting method. This approach enables not only smoothly varying impedance functions, but also varying cells with arbitrary shapes, sizes and direction of anisotropy as a function of position. The patterns in Fig. 2.7 were generated by starting function with a square grid. However, we have also developed code to start with a triangular grid, which can produce similar results, allowing a wider range of possible patterns. After having demonstrated the range of properties that are achievable with this method we now use it to create a simple example of a structure which requires a smoothly varying impedance profile, in the form of a planner Luneburg lens. We should note that our method is applicable to general tensor impedance

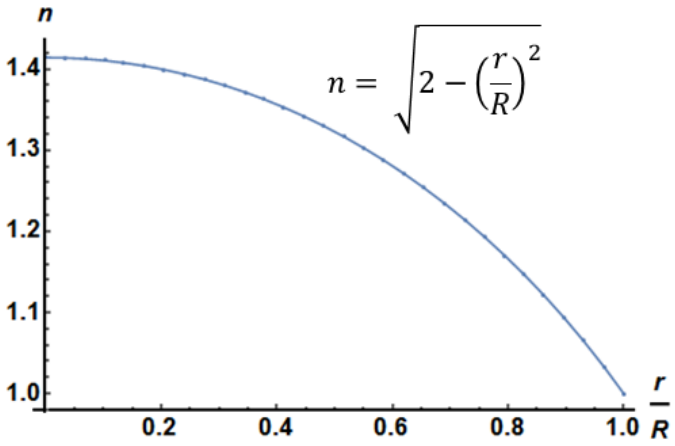

Figure 2.8: Index plot of Lunenurg lens

surfaces having a wide range of properties including anisotropy, as illustrated in fig. 2.7. However, since canonical anisotropic impedance surface problems are not widely known, for the purpose of demonstrating and validating our patterning method we choose a common problem with a well-defined solution that requires a smoothly varying surface impedance. For this reason we have selected a planar Luneburg lens design as an example.

2.3 Luneburg lens patterning

A Luneburg lens is a spherically symmetric gradient-index lens [16]. The refractive index n of the lens follows the function

$$n = \sqrt{\varepsilon_r} = \sqrt{2 - \left(\frac{r}{R}\right)^2} \tag{2.1}$$

where r is the radial distance from the center of the lens and R is the radius of the lens. The index n falls from $\sqrt{2}$ to 1 from the center to the edge. It has also been demonstrated in planar form using impedance surfaces [18, 19]. As an example of a practical application of our point shifting method, we generate an inhomogeneous impedance surface with the

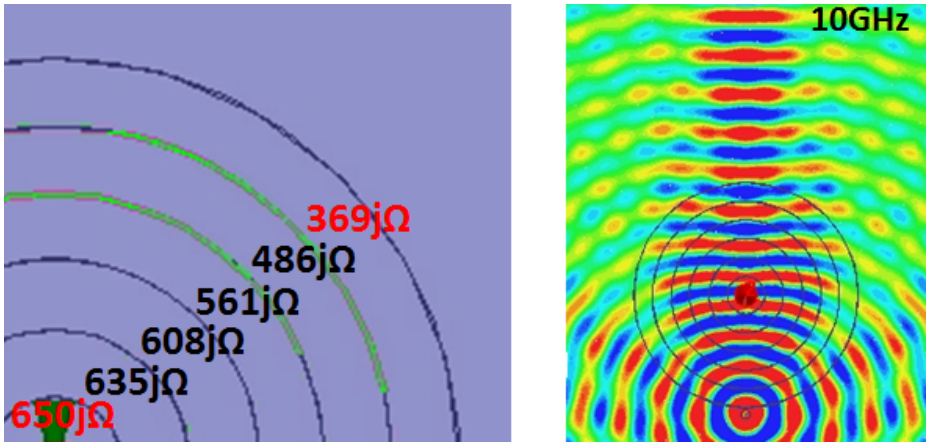

Figure 2.9: Normalized field plot from the impedance boundary simulation

Luneburg lens profile. We then simulate and measure it to verify that this approach can produce the intended impedance pattern.

2.3.1 Impedance boundary simulation

Before designing the impedance pattern of Luneburg lens, impedance boundaries have been simulated. The surface impedance of TM mode can be defined with effective TM index as [20]:

$$Z_{TM} = Z_0 \sqrt{1 - {n_{TM}}^2} \tag{2.2}$$

From the above Luneburg lens index plot we calculate surface impedances for boundaries. The diameter of the lens is 120mm and the impedance variation over boundaries from 369jΩ to 650jΩ follows the index plot. Fig. 2.9 shows a part of impedance boundary lens and a normalized field plot at 10GHz.

2.3.2 Unit cell simulation results and impedance data

The patterned Luneburg lens consists of patches which set the surface impedance. Therefore we first analyze the impedance as a function of cell geometry to determine the appropriate range of cell sizes for a given substrate and thickness. Assuming grounded 2.5mm thick Rogers 6010 substrate (ε_r = 10.2), we studied cells ranging in size from 1 mm to 5 mm, shown in Fig. 2.10. The gap was 0.25 mm for each case. Although the patches will have various shapes, we studied square patches as a compromise that is representative of a typical patch. We have previously shown that for anisotropic surfaces with rectangular unit cells, the impedance along one direction is independent of the cell size in the orthogonal direction [1], so simulations of square cells provide an understanding of the behavior of rectangular cells as well. The unit cell structure was simulated in the eigenmode solver in Ansys HFSS version 15.0.3 (a full-wave, commercial software package) The surface impedance for TM waves was calculated as

$$Z_{TM} = Z_0 \sqrt{1 - \left(\frac{k_{TM} c}{\omega}\right)^2} \tag{2.3}$$

based on the dispersion results of the unit cell [8, 21]. Fig. 2.10. shows the frequency-dependent surface impedance plot of unit cells from 1 1mm to 5 5mm. In this plot TM surface impedance can be translated to the index so that the analysis allows us to find an appropriate range of cells which follows the index profile of a Luneburg lens. The effective TM index for surface waves is defined as [20]:

$$n_s = \sqrt{1 - \left(\frac{Z_{TM}}{Z_0}\right)^2} \tag{2.4}$$

According to the simulation results we can find appropriate cell sizes which support

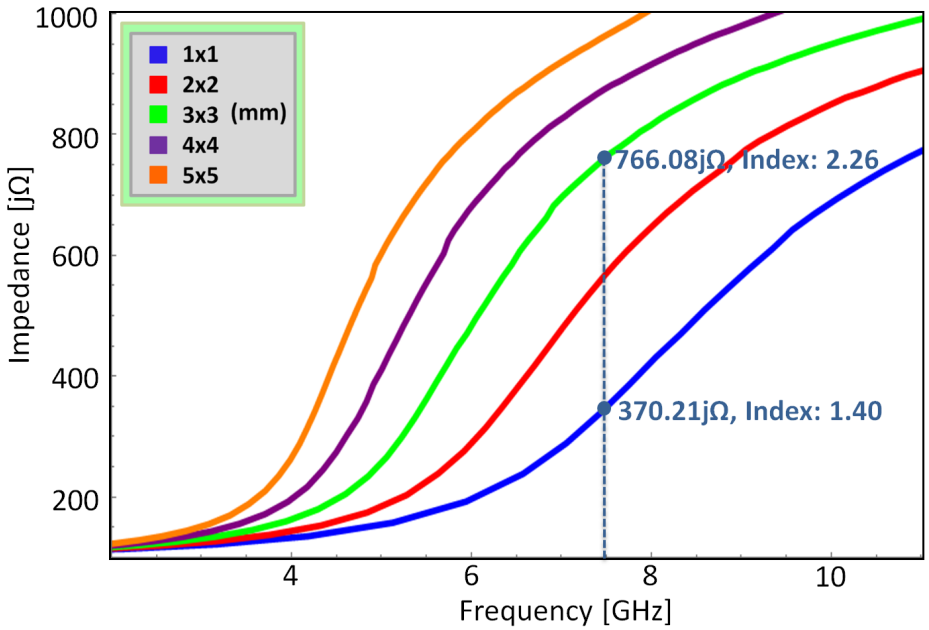

Figure 2.10: Impedance plot for various sizes of square unit cells. Simulated impedance versus frequency for various sizes of square unit cells on 2.5 mm Rogers 6010 with 0.25 mm gaps. The indicated impedance range of 766.08 jΩ to 370.21 jΩ corresponds to an index ratio of 1.6:1.

the surface impedance range for the Luneburg lens index at around 7 - 8.5GHz. Fig. 2.10 shows the result at 7.5GHz which is selected as the operating frequency of our Luneburg lens pattern. In order to approximate the Luneburg lens profile, we choose a range of cells varying from 1mm to 3mm, which corresponds to an impedance range of 370.21jΩ to 766.08jΩ. Using (2.4), this corresponds to an index ratio of approximately 1.6. The next step is to select a starting function for our pattern generation code which will produce a rotationally symmetric array of cells that vary smoothly from 3mm in the center to 1mm at the edges.

2.3.3 Patterns by point shifting method and simulation results

We do not have a direct method to produce an arbitrary impedance function. Instead, we begin with a function that has the appropriate properties for our intended application,

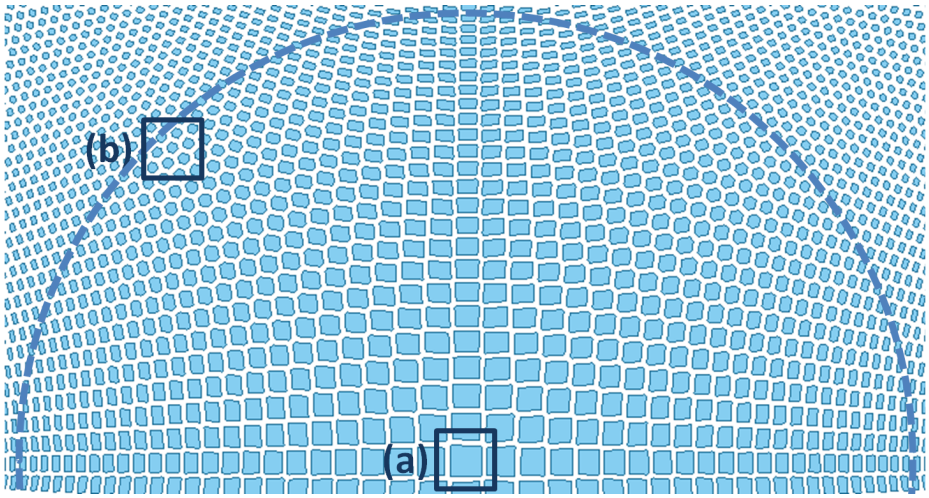

Figure 2.11: The Luneburg lens pattern used in the simulations. (only half shown) (a) Patches at the center of the lens measured 3 mm. (b) Patches at the edge of the lens measured 1 mm. These produce a 1.6:1 index ratio.

and then fit that function to produce the range of cell sizes that correspond to the desired impedance range. For example, a planar Luneburg lens requires a function with circular symmetry, and a local maximum in the center. The Luneburg lens pattern was generated by the point shifting method on a 93 $\times$ 93 point array with a starting function, f .

$$f = \sqrt{1000e^{-0.2(x^2+y^2)^{0.9}}} \tag{2.5}$$

This function was chosen empirically to generate a smoothly varying pattern of cells with rotational symmetry to approximate the Luneburg lens function. A section of the lens, and details of the unit cells from the center and edge are shown in Fig. 2.11. As shown in Fig. 2.10, the range of patch sizes varies from 1mm to 3mm from the edge to the center of the lens, and these sizes were chosen to provide an index ratio of 1.4 as required for the Luneberg lens profile. The substrate is the same 2.5 mm thick Rogers 6010 as used in the unit cell analysis. The diameter of the lens is approximately 90mm and the whole pattern dimensions are 140 $\times$ 140mm. The pattern consists of 8281 PEC patches

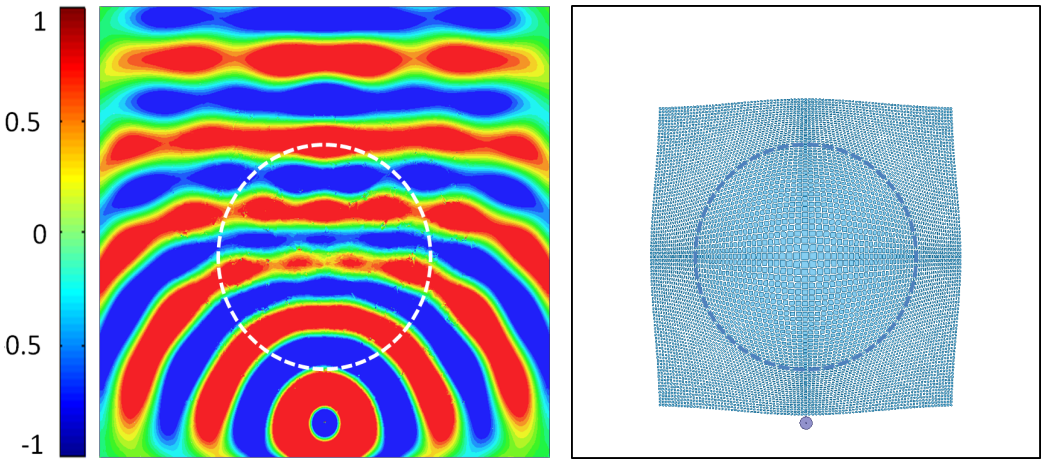

(a) (b)

Figure 2.12: Simulation result of the patterned Luneburg lens (a) Normalized electric field at 7.5GHz. Simulated data showing the field of a collimated surface wave produced from a monopole feed. (b) The area of the lens and surrounding board. The edge of the lens is approximate because it does not have a distinct boundary.

and there are 0.5mm gaps between the cells. This lens differs from the true Luneburg lens profile in several ways. First, it does not match the function in (2.1) exactly, it is only an approximation. Second, it does not have a distinct edge, as the cells simply get smaller away from the center at a rate that exponentially approaches the background cell size of approximately 1mm. Nonetheless, we can define an approximate edge to roughly match the edge of the Luneburg lens function. Third, the cells end about 2cm past the edge of the lens, and the surrounding material is dielectric clad ground plane, with an impedance of 75.5jΩ [22]. In spite of these differences, this approach has the advantage that the index varies smoothly, aside from the discrete nature of the cells, and we do not need to use shells or rings as in some other planar lens structures [23].

The Luneburg lens pattern was simulated using the driven modal solver in Ansys HFSS. Fig. 2.12 shows the field plot at 2mm above the board at 7.5GHz. There is a coaxial feed in front of the pattern which generates circular waves that propagate over the lens

pattern. The wavefronts are flattened as they pass through the lens pattern. As shown in this figure, the printed impedance surface produces a collimated beam at the output of the lens, as expected, validating our patterning procedure.

2.4 Beam shifting patterning

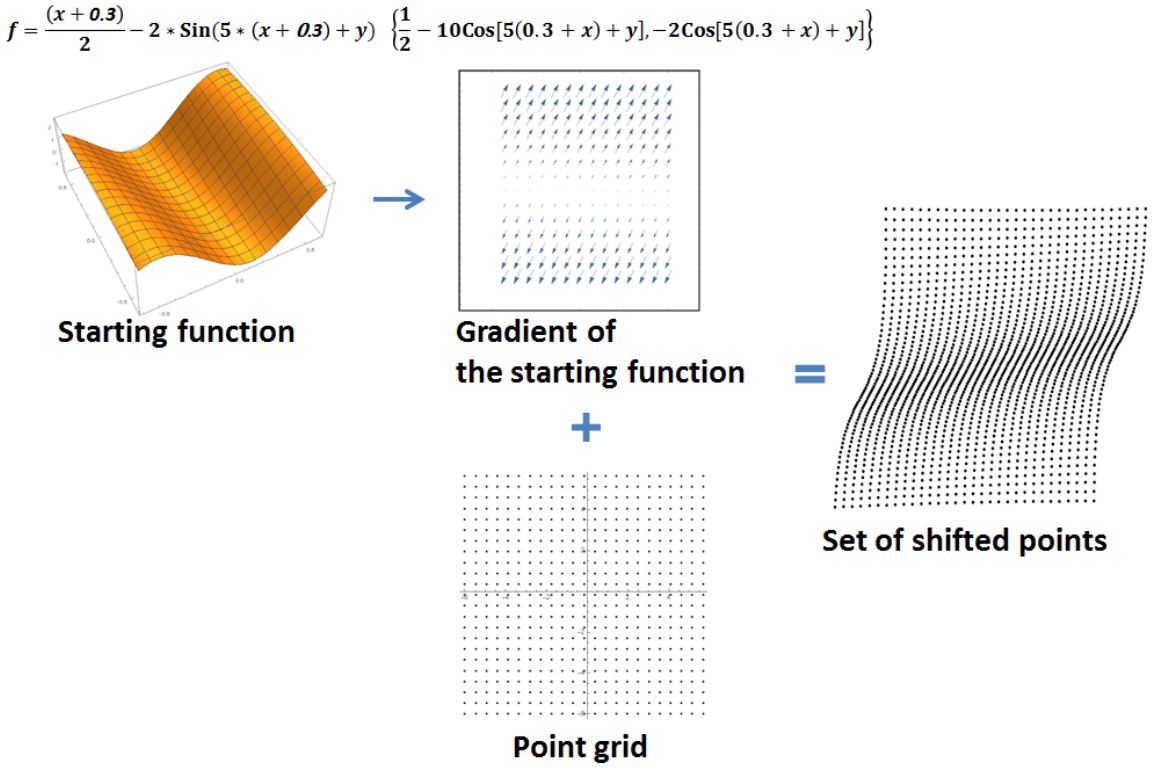

Figure 2.13: Procedure of designing a beam shifting pattern

In addition to the lens, we have also studied a structure that explicitly requires anisotropy, to demonstrate the usefulness of this structure for generating anisotropic patterns. As an example, we have designed a beam shifting strucutre. Such structures have been designed prevoiusly using anisotropic metasurfaces [3]. However, prevoius work involved homogenoius impedance surfaces because of the difficulty of patterning inhomogenoius anisotropic surfaces. The beam shifter can be understood by considering that waves in an

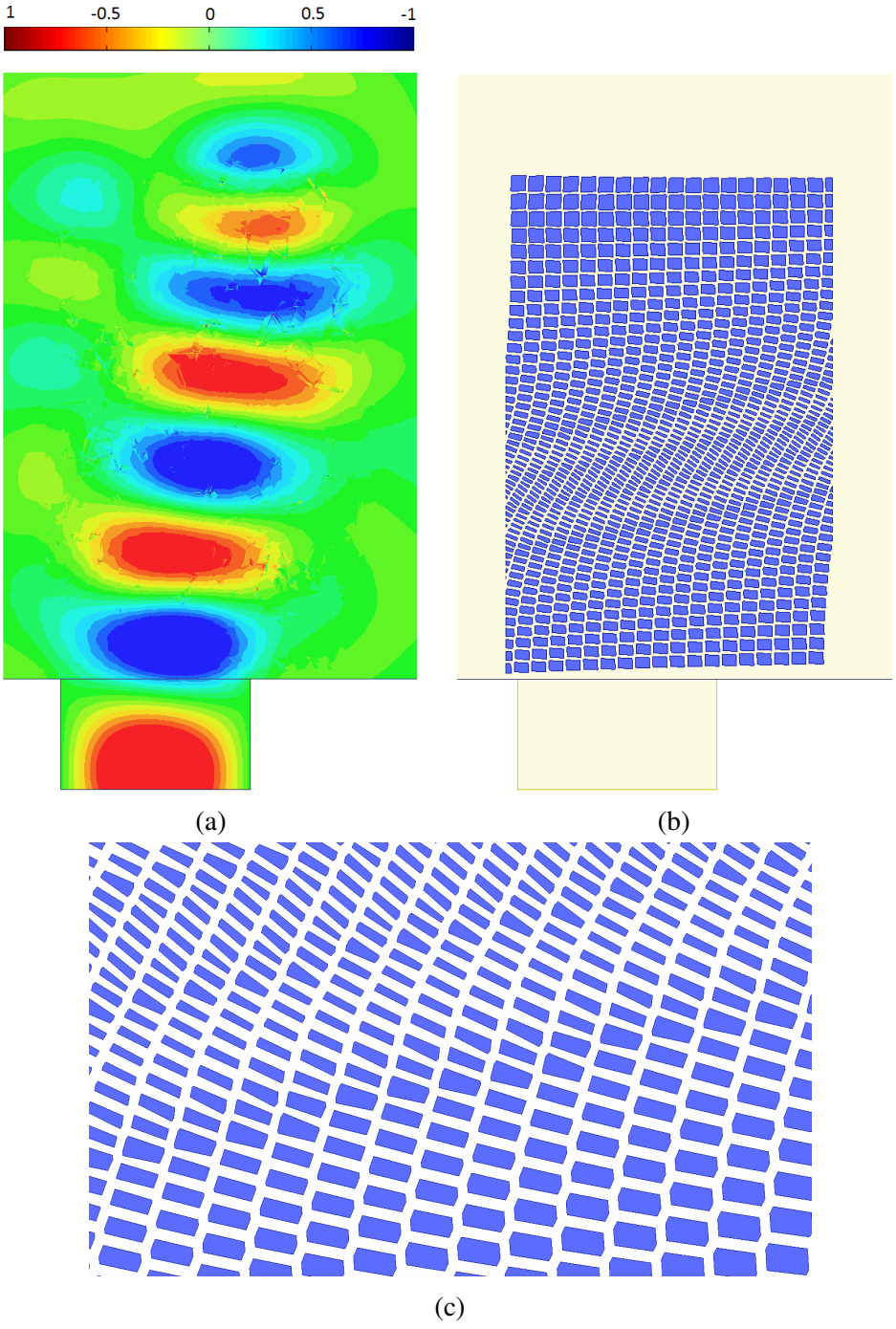

Figure 2.14: Simulation result of the beamshifter. (a) Normalized electric field at 7GHz. (b) Pattern on the board with a wave guide source. (c) Enlarged section of the beam shifting surface.

anisotropic medium will refract toward the lower index direction [24]. By gradually tilting the direction of low impedance, the wave can be made to follow a desired path.

The beam shifting pattern was generated with starting funtion, f.

$$f = \frac{x}{2} - 2\sin(5x + y) \tag{2.6}$$

The patterning method resulted in 1154 PEC patches which were printed on a grounded 2.5mm thick Rogers 6010 substrate. The size of the entire structure 56mm $\times$ 88mm. For the elongated patches near the center of the beam shifting structure, the impedance was 260 jΩ in the low direction, and 374 jΩ in the high direction. Simulations, shown in Fig. 2.14, indicate that a beam excited at one end of the structure (such as generated by a waveguide aperture) will be shifted by nearly an entire beamwidth at the other end of the structure. This smoothly varying beam shifting structure represents a pattern that would be impossible to produce using existing techniques. The performance of both the Luneburg lens and the beam shifting surface were verified experimentally, as described in the following section.

2.5 Near field scanning measurement

The Luneburg lens pattern was fabricated using printed circuit fabrication technology, and is shown in Fig. 2.15. The panel is 190 $\times$ 180 mm with 8281 copper patches on top of the board, and bottom of the board is a ground. There is a 5mm diameter hole in front of the pattern for a coaxial feed which is the excitation source. A vertical probe was swept 2mm above the surface along a 1mm grid and an Agilent E5071C vector network analyzer recorded the magnitude and the phase of the surface wave. Normalized field results are

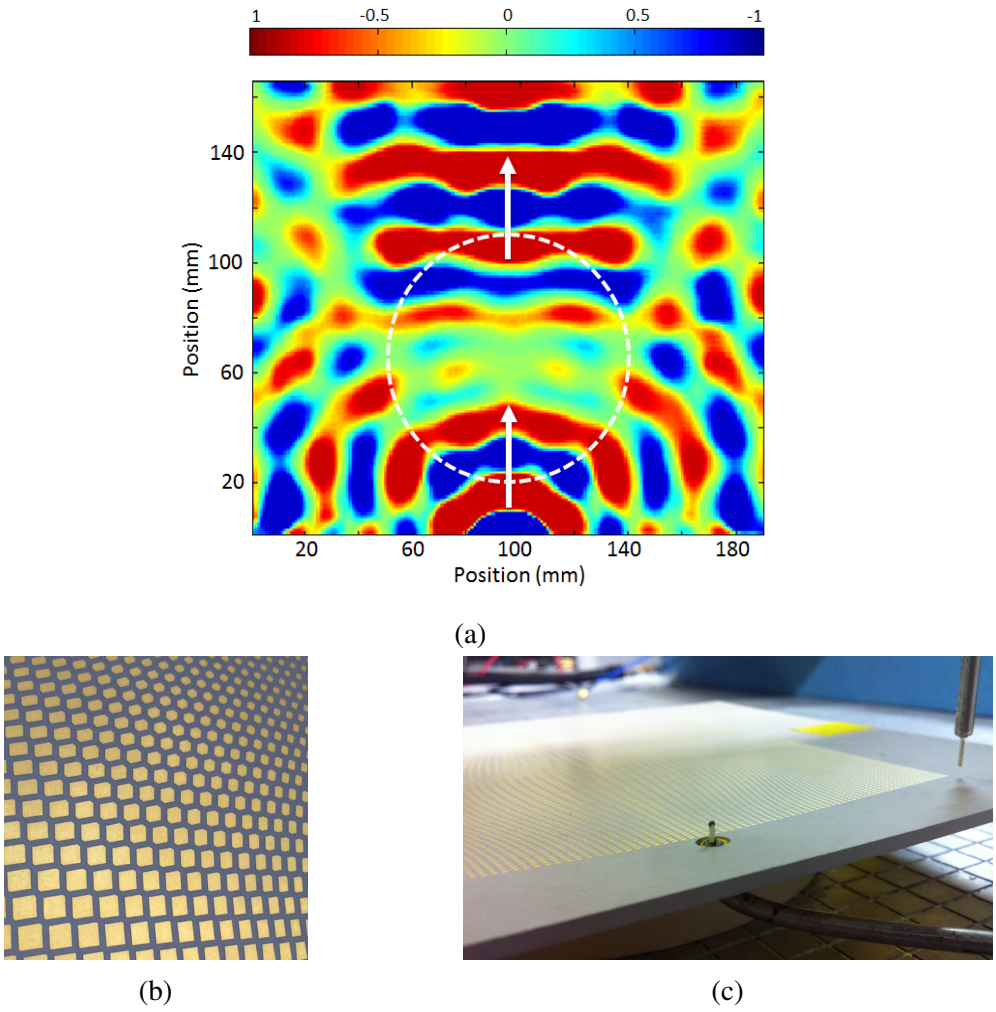

Figure 2.15: Measured fields of the patterned Luneburg lens (a) Normalized near field plot of the surface waves scanned over a 190 165 mm area, indicating the collimating capabilities of the lens. The scan starts just beyond the feed point. (b) Close-up photo of the fabricated Luneburg lens pattern. (c) Details of the feed and the measurement technique, including the probe visible at one extreme of the scan region.

shown in Fig. 2.15(a). The circular wavefronts generated by the feed are transformed into flat wavefronts at the opposite side of the lens, as expected. The essential characteristics of the pattern match that shown in Fig. 2.12, verifying that our technique produces practical impedance surface patterns that match simulation results, and perform a useful function of collimating surface waves. The flat wavefronts emerging from the surface of the lens opposite to the feed are the expected behavior for a Luneburg lens. The additional variations along the edges of the measurement area are artifacts that are indicative of a standing wave pattern which is likely caused by reflections from the edges of the board. The beam shifting

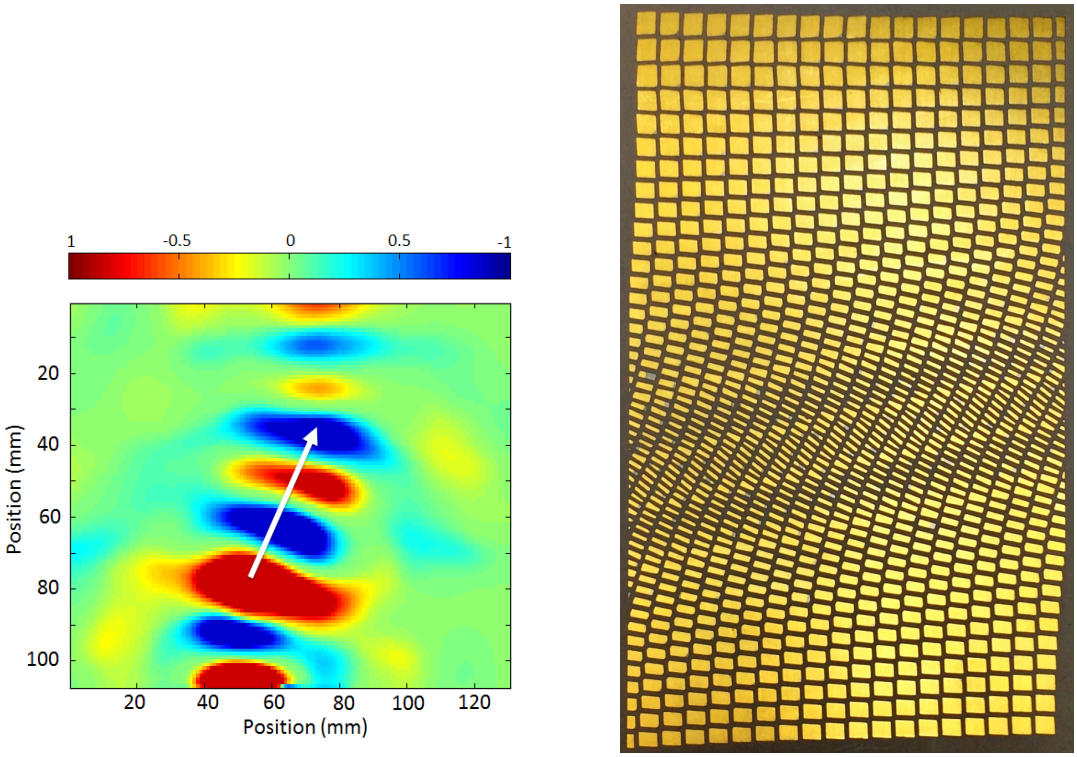

(a) (b)

Figure 2.16: Measured fields of the beamshifter (a) Normalized electric field at 7GHz. (b) Pattern on the board with a wave guide source. (c) Enlarged section of the beam shifting surface.

structure was excited by a WR137 waveguide placed adjacent to the surface at one edge. A field map was produced in the same way as for the lens described above, and is plotted in

Fig. 2.16. The beam center is smoothly shifted from 50 mm to 70 mm along the length of the structure. Note also that the phase fronts begin and end parallel to the front and back edges of the surface, gradually tilt to the right in the central region, following the anisotropic impedance pattern.

2.6 Conclusion

We have introduced a patterning technique for generating arbitrary impedance surfaces. It provides several advantages over other patterning approaches such as the ability to produce a range of cell sizes, shapes, and orientations, including smoothly varying and highly anisotropic impedance surfaces. Specifically, the ability to produce smoothly varying impedance surfaces with reduced symmetry cells, which are important for achieving high anisotropy, has been absent from all previous patterning methods. We have illustrated the limitations of existing techniques, as well as other potential approaches such as conformal mapping, and path-dependent methods. We have shown that our technique based on point shifting with Voronoi cell generation can produce impedance surfaces with a wide range of useful properties. We have chosen a simple and practical example to validate our method experimentally, in the form of a planar Luneburg lens as well as an anisotropic beam shifting structure.

We expect that this method will be used to design a wide range of future impedance surface for applications such as planar antennas, scattering control, and interference mitigation. However, there are also several fundamental questions that are topics for future research. First, the starting function is currently chosen empirically to produce a described range of predetermined cell geometries. We need a method to translate the desired impedance function directly to the starting function. Second, the limitations of this method are not

known, such as the range of impedance functions that are achievable. Third, aside from certain special cases such as the lens illustrated here, it is not known what impedance function is required to produce a specific surface wave or scattering response. Addressing these issues will allow us to use the method described here to produce arbitrary impedance surfaces for a wide range of applications.

Chapter 2 is based on and is mostly a reprint of the following paper: **J. Lee**, D. Sievenpiper, "Patterning Technique for Generating Arbitrary Anisotropic Impedance Surfaces", *IEEE Transactions on Antennas and Propagation*, vol. **64**, no. 11, pp. 4725-4732, December 2016. The dissertation author was the primary author of this material.

Chapter 3

Scattering Reduction Scheme using Impedance Surfaces

3.1 Motivation

Controlling surface waves is important to prevent damage to sensitive spots on the surface or to minimize interference with other systems. As shown in Fig. 1.2 in Chapter 1, if the aircraft has multiple sensitive regions on the surface and an incident wave hits the aircraft, either the flow of surface waves should be guided in the other direction avoiding spots or the sensitive area should be shielded from the wave.

To solve this problem there are several approaches have been tried such as cloaking techniques from transformation electromagnetics and beam shifting methods. However some of transformation methods cannot be implemented for surface wave structures since it is not possible to independently set the impedance and index in the material in two dimension impedance surfaces unlike volumetric materials. Also impedance surfaces don't have freedom in setting tensor solutions of ε and μ in the tensor impedance boundary

condition and have only three independent variables, Z_{xx}, Z_{yy}, Z_{xy}, which can be set.

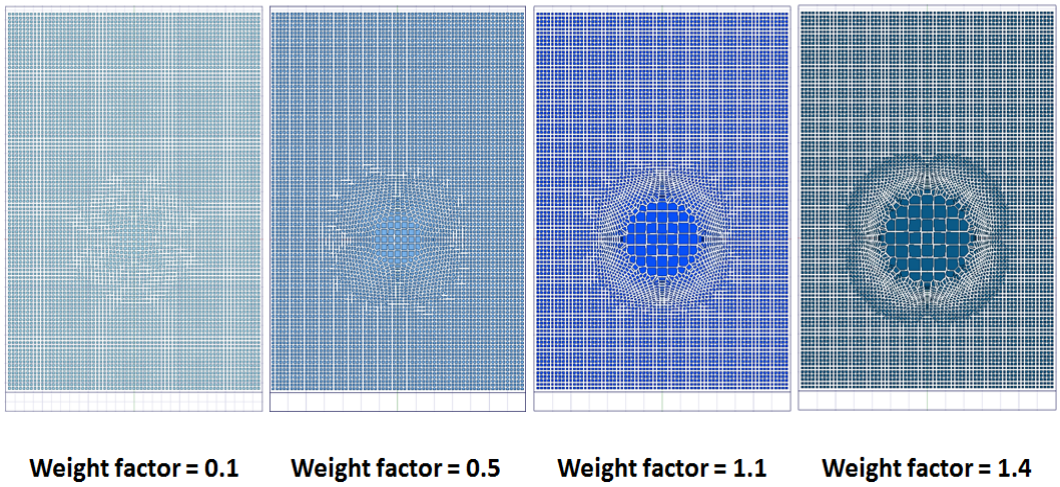

(a)

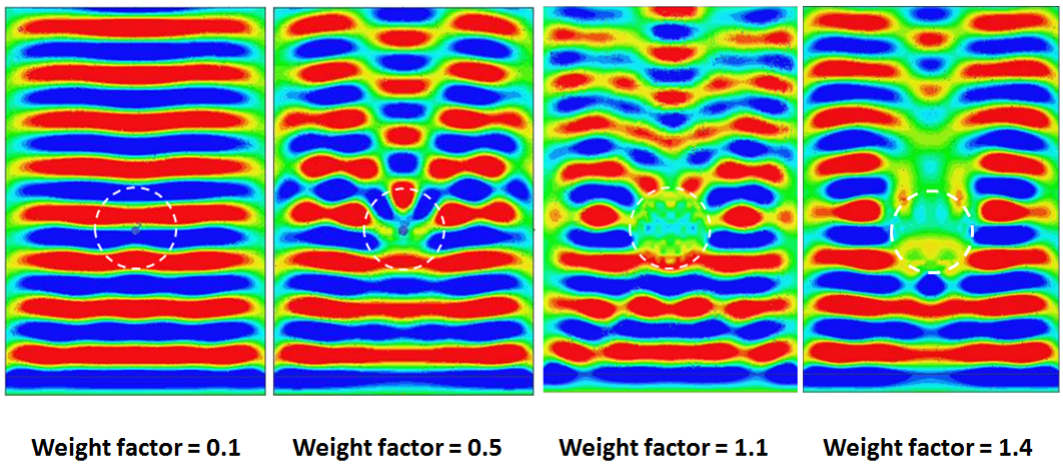

(b)

Figure 3.1: Impedance patterns with different weight factors

3.2 Surface wave shielding pattern design

The idea of surface wave shielding pattern is applying higher surface impedances to the shielded area comparing with surface impedances in the background, and having smooth transition between low and high impedance region. Fig. 3.1(a) shows impedance surfaces

generated by the point shifting method. A convex function in three dimensional space is used as a starting function for patterning and applied with various weight factors. As shown in 3.1(b) the surface wave starts being suppressed when the pattern has larger unit cells at the center than background unit cells so that high impedance area has emerged in the middle of the pattern.

The third pattern with weight factor 1.1 in Fig. 3.1(a) shows high impedance region at the center of the pattern and it is surround by smooth transition to low impedance background. The unit cell size of highest impedance is 4mm $\times$ 4mm which is 6 times larger than background unit cells. The normalized field plot in Fig. 3.1(b) shows the shielded area from the wave in the middle of the pattern, and the wave keep propagating beyond the high impedance area and recombine.

Fig. 3.2 shows comparison between a full shielding pattern and other shielding conditions. In Fig. 3.2(a), all three impedance surfaces have huge jump from low impedance at the background to high impedance in the center which is the shielded area. The first structure is a fully patterned impedance surface with PEC patches on the 2mm thick Rogers 3010 substrate. The second structure has same condition with the first structure except the background unit cells including smooth transition area. Here the background unit cells and the transition area are removed. The impedance surface consists of the same Rogers 3010 substrate and a few PEC patches in the middle which have high surface impedances. In the third structure low impedance unit cells in the background remain, but the high impedance region is replaced by one piece of PEC patch and the transition area is removed.

Fig. 3.2(b) shows normalized field plots of three different shielding conditions at 9GHz. The fully patterned impedance surface shows a clear shielded area from the surface wave at the center of the plane. In the second structure the high impedance region shows

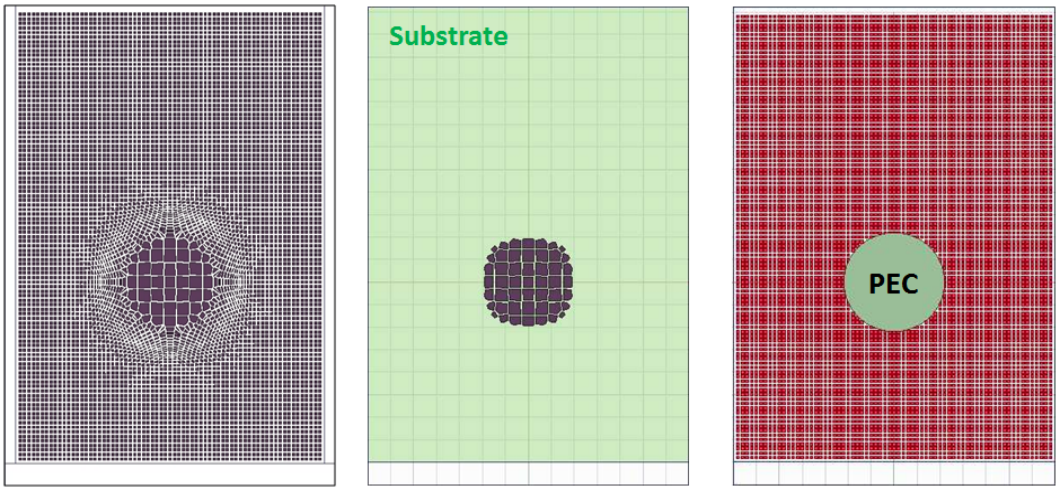

(a)

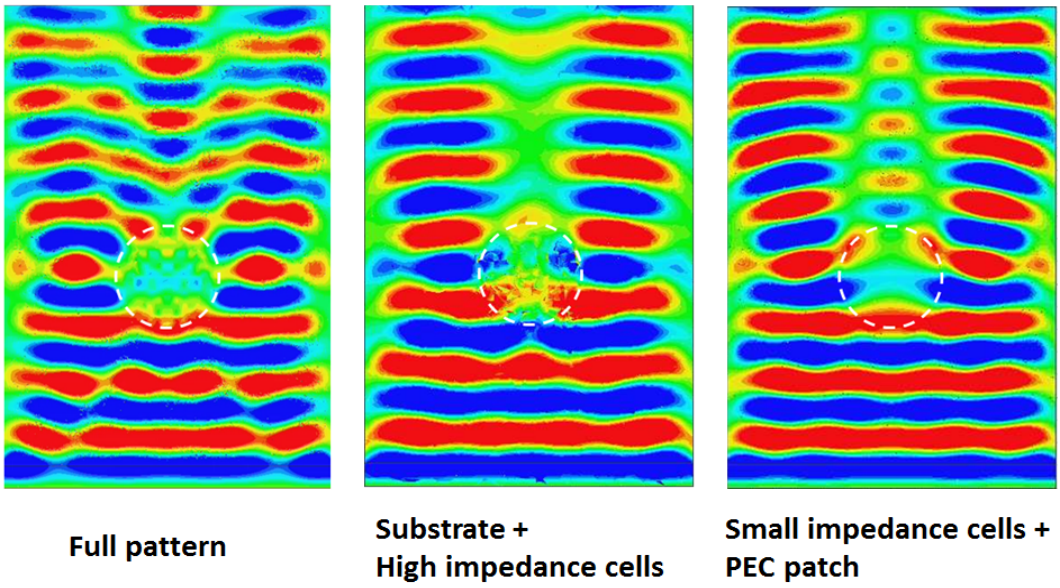

(b)

Figure 3.2: Comparing a full shielding pattern with other conditions.

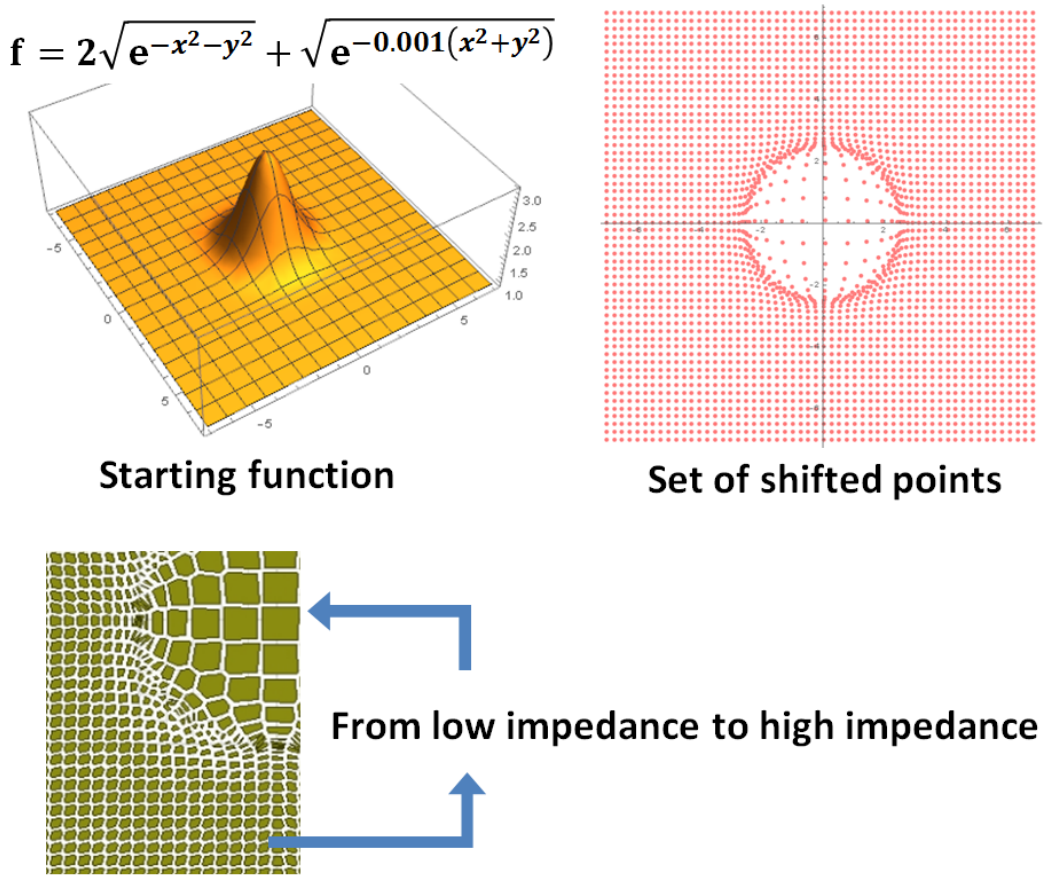

Figure 3.3: Procedure of designing a shielding pattern. A starting function plot and set of shifted points.

reflections around the patches and couldn't stop the wave coming into the area. The third structure shows the wave is weakened in the PEC patch but the surface waves are out of phase after passing the high impedance region.

Fig. 3.3 shows a starting function and set of shifted points for a shielding pattern. The pattern is design to have the larger shielded area than the previous pattern shown in Fig. 3.1 and Fig. 3.2. A full shielding pattern and a normalized field plot at 9.2GHz are shown in Fig. 3.2.The diameter of the shielded area is approximately 60mm including the transition region. The pattern is simulated with a plane wave source. In the field plot we

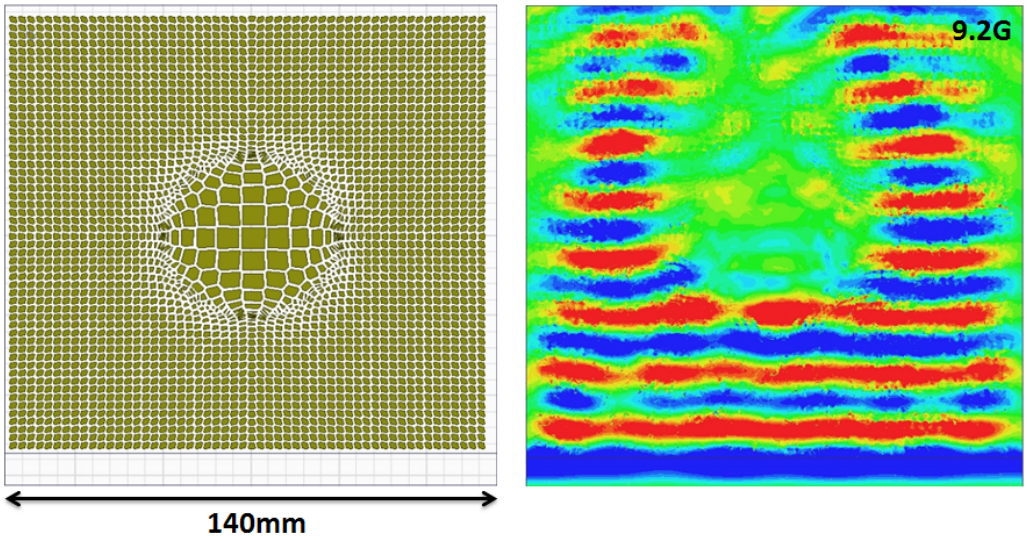

Figure 3.4: A shielding pattern and normalized field plot at 9.2GHz

can observe that the surface wave is blocked and shows lower magnitude in the high surface impedance region with larger patches.

Fig. 3.5 is the simulation results of the shielding pattern with waveguides. The field plots show the surface wave propagates over the pattern avoiding the shielded area, and the wave smoothly flows around the transition area without significant reflections.

3.3 Preventing Leakage of surface waves by smooth varying impedance pattern

We have applied the shielding pattern to prevent or reduce the leakage of surface waves from a slot or a crack on the object. This approach can be useful in certain situations when the traveling waves hit the object such as aircrafts or cars which have windows or slits on their body.

Fig. 3.6 shows a design of the pattern and structure. A 12 $\times$ 32 mm slot is located in the middle of a 2mm thick Rogers 3010 substrate. The diameter of the shielded area in the

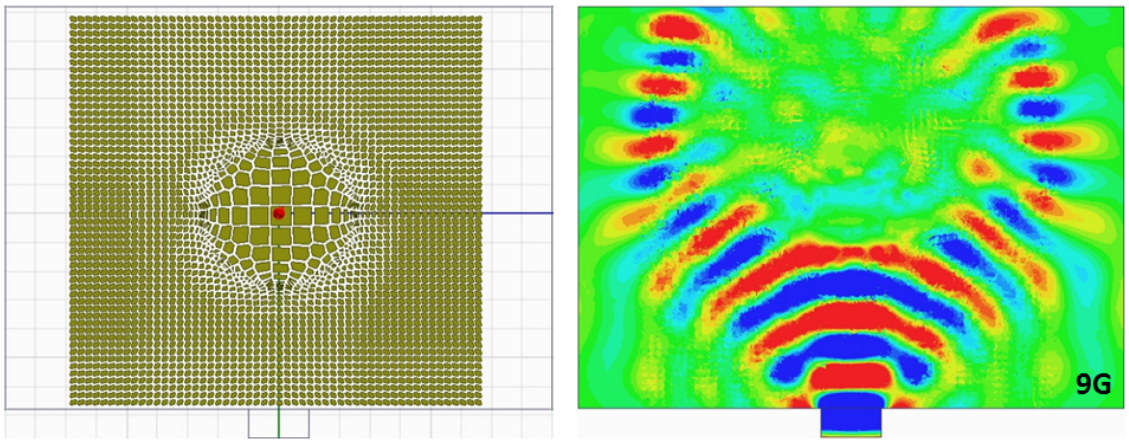

(a)

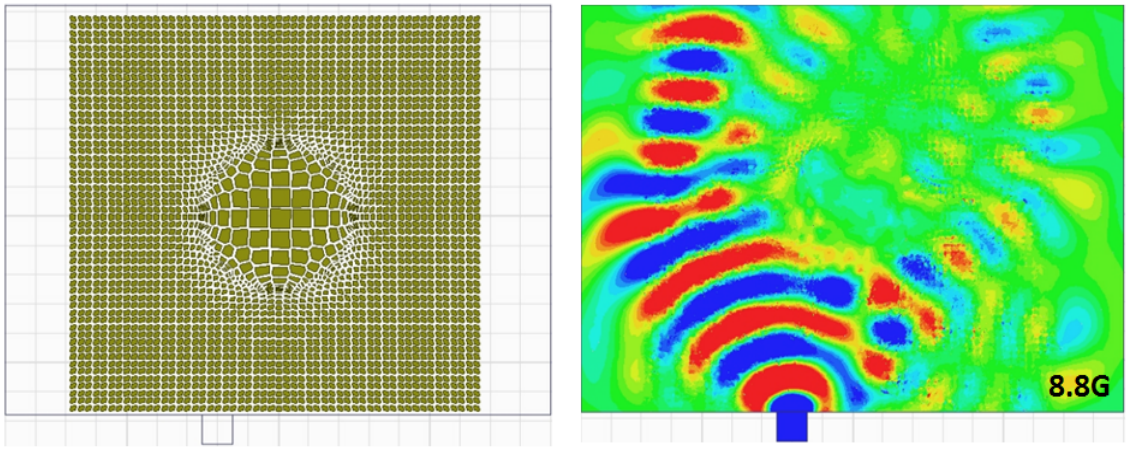

(b)

Figure 3.5: Shielding pattern and normalized field plot with rectangle wave guides (a) Normalized field plot at 9GHz (b) Normalized field plot at 8.8GHz. The source is located at the left bottom of the pattern.

pattern is 90mm. We simulate the board patterned with PEC patches and a plane substrate board without the pattern. The surface waves from the source are propagating around the shielded area and couldn't flow into the As shown in the normalized field plot in Fig. 3.6 there is no leakage wave from the slot when the board has covered with a shielding pattern.

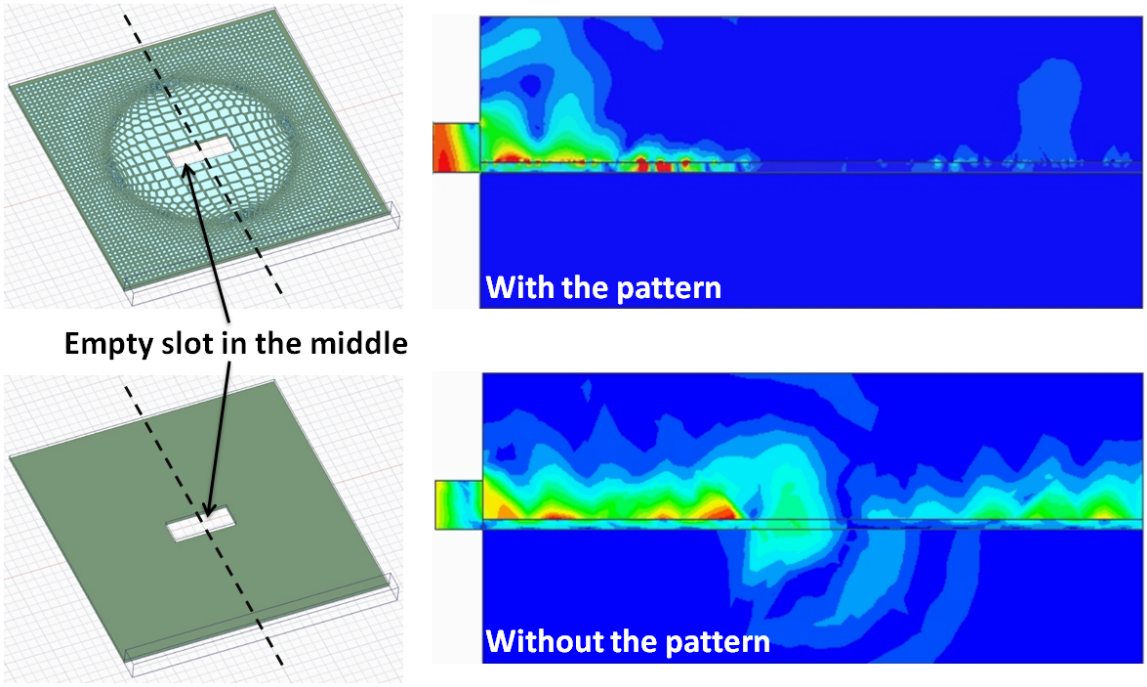

Figure 3.6: Manually designed anisotropic impedance surface

3.4 Conclusion

This chapter has demonstrated a pattern that can be used for shielding two dimensional area from surface waves. We've studied several designs of high and low surface impedances combination for surface waves shielding. The surface waves on the full pattern propagate around the shield area which is covered by larger PEC patches that have high surface impedances. We have also simulated substrate boards with a slot and showed the leakage of surface waves are prevented by the smoothly varying surface impedance pattern.

Chapter 3, in part, are currently being prepared for submission for publication of the material as it may appear in: **J. Lee**, D. Sievenpiper, Design of Arbitrary Anisotropic Impedance Surface for Reducing Leakage of Surface Wave. The dissertation author was the primary author of this material.

Chapter 4

Method for Extracting the Effective Tensor Surface Impedance

4.1 Motivation

To address the limitation of conventional artificial impedance surfaces, a patterning technique which is called the point shifting method [25] has been developed. Fig. 4.1 shows that impedance surfaces produced by the point shifting method have smoothly varying anisotropic patterns with various shapes of unit cells which vary over the surface along with the impedance values. Previously, we assumed that the impedances of polygon patches produced by the point shifting method can be represented by the tensor impedance of rectangular or square unit cells as an approximation. However, as the unit cells created by the point shifting method are highly asymmetric and polygonal, their shapes are sufficiently different from rectangles that we cannot accurately determine their surface impedance using this assumption. Additionally as the unit cells smoothly vary their orientations, the tensor impedance of each cell changes according to the tilt angle. For these reasons, we have

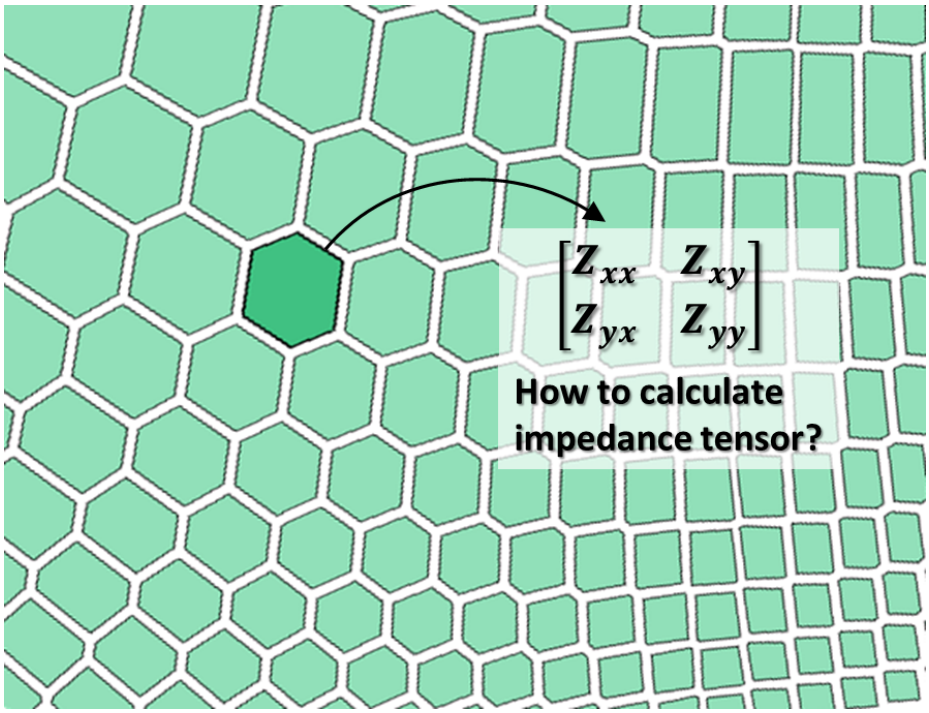

Figure 4.1: Arbitrary anisotropic impedance surfaces generated by the point shifting method. The unit cells of the pattern have all different shapes and sizes.

developed a technique to accurately calculate tensor impedances for various shapes and directions of polygon cells.

In this section, we introduce a new method to extract surface impedances from arbitrarily shaped patch cells using the moment of inertia equations. We discuss the details of the extraction process and provide an example of calculation for a polygon unit cell. We verified that the extracted surface impedances of polygon unit cells are in the reasonable range by comparing the simulation results between a PEC pattern and an impedance boundary sheet. Measurements show that the field profile matches the simulations, verifying that this method produces the intended impedance profile.

4.2 Extracting Surface impedance of nonuniform unit cell

Surface impedance is related with the geometry of a unit cell, and specifically depends on the length in the propagation dimension when the unit cell is a rectangle. [26] Our goal is to find an equivalent rectangle which has the same tensor impedance properties of a general polygon unit cell in the surface impedance patterns to extract accurate surface impedances in a convenient way. We take this approach because the impedance properties of rectangular cells can be calculated easily using periodic boundary conditions, while more complex or less symmetrical cells cannot be arranged into periodic boundaries. In calculating the impedance of the equivalent rectangular cell, we assume it is in an infinite homogeneous surface consisting of identical cells. Thus, assigning this equivalent surface impedance to a general polygon unit cell corresponds to the local impedance at that cell, which is actually part of a spatially varying impedance function. The use of an impedance function based on the local impedance values corresponding to individual unit cells has been established previously in the work on holographic impedance surfaces [9, 27].

4.2.1 Inertia of momentum

In attempting to define a function that relates the impedance tensor to the unit cell shape, we found that the impedance of a rectangular lattice is higher in the direction in which the cells are longer, and we observe that this is similar to the mechanical moment of inertial of a flat rectangular plate, which is higher when it is rotated around the short axis. In this work, we define the equivalent rectangle of the polygon unit cell as the rectangle having the same second moment of inertia [28] with the polygon unit cell. We note that this technique has been applied to limited patch style cells since other type of unit cells, such as active unit cells or patches with vias, have additional factors which determine their surface

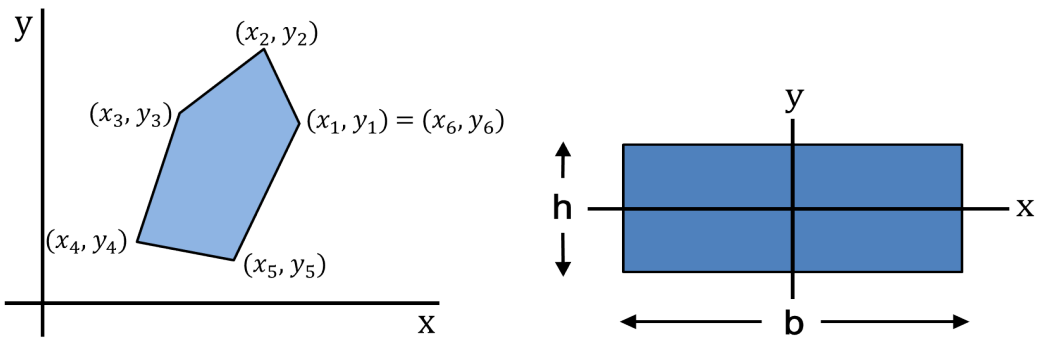

(a) (b)

Figure 4.2: A polygon and a rectangle for the moment of inertia equations are placed on a cartesian coordinate. (a) Numbering of vertices is counterclockwise. (b) A rectangle is located at the center of the coordinate. H is the length and b is the width.

impedances besides the geometrical dimensions of the patches or the gaps between cells.

The concept of the moment of inertia was borrowed to calculate the equivalent rectangular cell because it can explain the geometrical property of an area regarding directions and weight of the cell. Fig. 4.2 shows a polygon and a rectangle in cartesian coordinates, of which the second moment of inertia for the polygon is obtained from the locations of the vertices, given by

$$I_x = \frac{1}{12}\sum_{i=1}^{i=N}\left(y_i^2 + y_i y_{i+1} + y_{i+1}^2\right)\left(x_i y_{i+1} - x_{i+1} y_i\right) \tag{4.1}$$

$$I_y = \frac{1}{12}\sum_{i=1}^{i=N}\left(x_i^2 + x_i x_{i+1} + x_{i+1}^2\right)\left(x_i y_{i+1} - x_{i+1} y_i\right) \tag{4.2}$$

$$I_{xy} = \frac{1}{24}\sum_{i=1}^{i=N}\left(x_i y_{i+1} + 2x_i y_i + 2x_{i+1} y_{i+1} + x_{i+1} y_i\right)\left(x_i y_{i+1} - x_{i+1} y_i\right) \tag{4.3}$$

and for the rectangle is given by

$$I_x = \int_A y^2 dA = \int_{-\frac{b}{2}}^{\frac{b}{2}} \int_{-\frac{h}{2}}^{\frac{h}{2}} y^2 dy dx = \int_{-\frac{b}{2}}^{\frac{b}{2}} \frac{1}{3}\frac{h^3}{4} dx = \frac{bh^3}{12} \tag{4.4}$$

$$I_y = \int_A x^2 dA = \int_{-\frac{b}{2}}^{\frac{b}{2}} \int_{-\frac{h}{2}}^{\frac{h}{2}} x^2 dy dx = \int_{-\frac{b}{2}}^{\frac{b}{2}} hx^2 dx = \frac{b^3 h}{12} \tag{4.5}$$

The variable N in (4.1) - (4.3) is a number of vertices of the polygon. The second moments of area of simple polygons on the XY-plane are calculated by summing contributions from each segment of the polygon. We note that the coefficient 1/12 is a common coefficient from each term of the equation which is computed by the definition of the second moment of area regardless of the number of polygons sides.

4.2.2 Procedure of finding equivalent rectangle cell

Fig. 4.3 shows a procedure of calculating an equivalent rectangle which has the same impedance tensor as that of the polygon. A diamond shaped unit cell is used as an example polygon in Fig. 4.3, because the impedance tensor of both of these shapes can be solved using periodic boundaries, thus we can verify the approach. As shown in (4.1) - (4.3) and Fig. 4.2(a), not only the shape (position of vertices) and size of polygon but also its location on the x-y plane affects on the moment of inertia. Therefore, we set a centroid of the polygon as the zero point of the x and y axes first, shown as a red dot in Fig. 4.3(a) before calculating the moment of inertia. Once the moment of inertia matrix I is calculated from (4.1) - (4.3), we find the eigenvalues and eigenvectors of the matrix I. Since the eigenvalues of matrix I mean Ixx and Iyy of the diamond cell when the cell is perpendicular to axes, we apply these two values to (4.4) and (4.5) by definition of the equivalent rectangle. From (4.4) and (4.5), we can find a length and a width of the equivalent rectangle as shown in

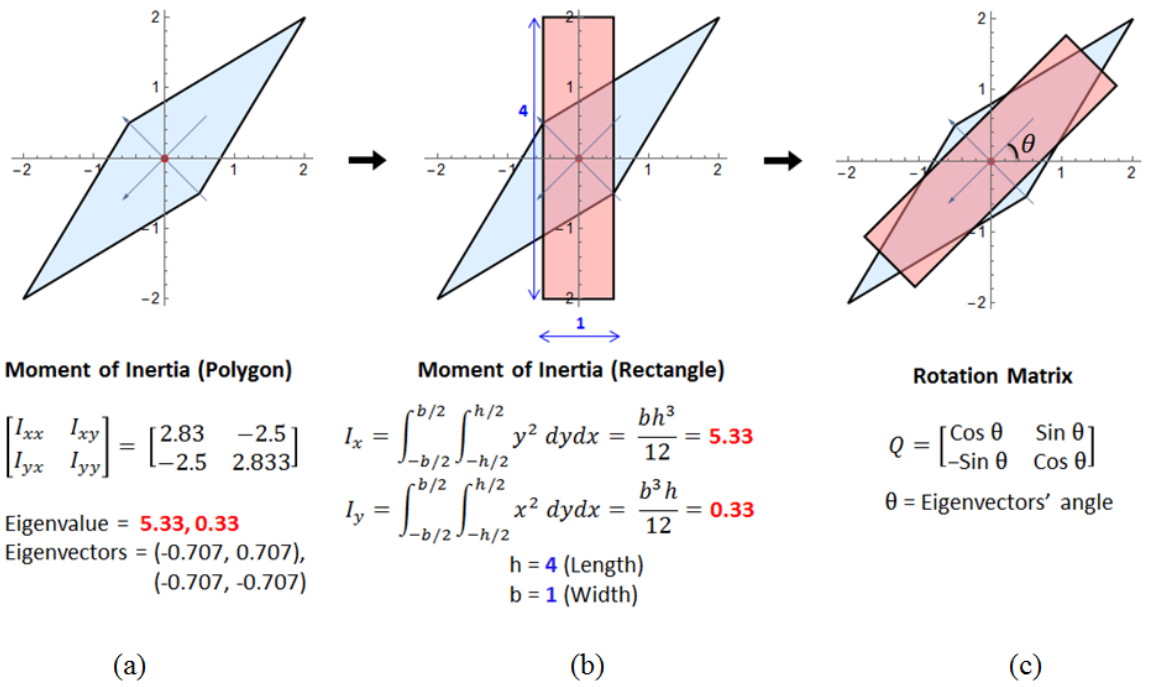

Figure 4.3: Procedure of calculating equivalent rectangle. (a) A polygon unit cell and centroid (a red dot) at the zero point. (b) An equivalent rectangle is calculated by the relationship between eigenvalues of the moment of inertia matrix for the polygon and the second moment of inertia of rectangle. (c) The equivalent rectangle tilted by the angle. is the rotated angle which is calculated from eigenvectors of the moment of inertia matrix for the polygon.

Fig. 4.3(b). Fig. 4.3(c) shows the tilted equivalent rectangle by , which is the angle of the polygon from x axis. The angle is calculated from eigenvectors of the polygon which is -45 degrees in the example. Fig. 4.4 is a top view of polygon and rectangle cells for eigenmode simulations in Ansys HFSS version 18.2 (a full-wave, commercial software package). We assign 0.25mm gaps on the cell so that the gap width between patches is 0.5mm as shown in the diamond cell. Dashed lines in the diamond cell present the original size which has shown in Fig. 4.3(a).

Fig. 4.5 is a plot of the surface impedance for rectangular cells which are analyzed as a function of cell geometry for a given substrate, thickness, frequency and gap between patches. The rectangular unit cell structure was simulated by changing both its longitudinal

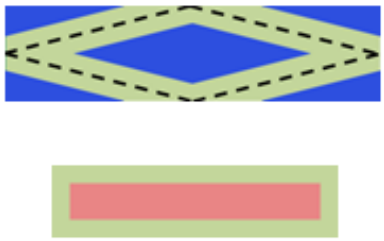

Figure 4.4: Polygon unit cell and its equivalent rectangle. Top view of polygon and rectangle cells for eigenmode simulations in HFSS. Polygon cell dimension is $4\sqrt{2} \times \sqrt{2}$ mm and the equivalent rectangle is 4×1 mm with 0.25mm gaps. (0.5mm gap width between patches) Structures are surrounded by two pairs of periodic boundaries.

and transverse length in the eigenmode solver in HFSS. The surface impedance for TM waves was calculated as

$$Z_{TM} = Z_0 \sqrt{1 - \left(\frac{k_{TM} c}{\omega}\right)^2} \tag{4.6}$$

Although the surface impedances of a rectangular unit cell are mainly affected by the length in the propagation direction [26], there is still some dependence on the transverse dimension. This can be ignored in periodic rectangular cell patterns, however here we consider the impedance variation due to the transverse length as well for the accuracy of the tensor impedance of a smoothly varying impedance pattern [29]. According to the graph in Fig. 4.5 which is for rectanfular cells on a grounded 2.5mm thick Rogers 6010 substrate (ε_r = 10.2) with 0.25mm gap, a tensor impedance matrix of the equivalent rectangle, Z_{ER}, for 41mm size (from Fig. 4.3(b)) at 7GHz is

$$Z_{ER} = \begin{bmatrix} Z_{xx} & Z_{xy} \\ Z_{yx} & Z_{yy} \end{bmatrix} = \begin{bmatrix} 292.64 & 0 \\ 0 & 790.64 \end{bmatrix} j\Omega \tag{4.7}$$

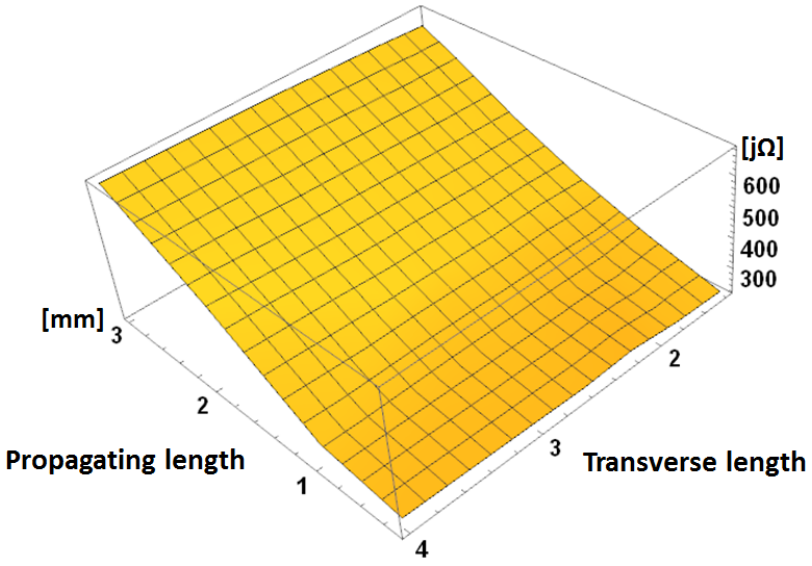

Figure 4.5: Impedance plots. Simulated impedance versus propagating lengths and transverse lengths at 7GHz for rectangle unit cells on 2.5 mm Rogers 6010 with 0.25 mm gaps.

Once Z_{ER} is obtained from the surface impedance graph, we need to rotate the impedance tensor to fully represent the polygon in its coordinate system. In order to keep the properties of equivalent rectangle in the matrix, we use Jacobi rotation where the rotation matrix Q [30] is

$$Q = \begin{bmatrix} Cos\theta & Sin\theta \\ -Sin\theta & Cos\theta \end{bmatrix} \tag{4.8}$$

Therefore, a tensor impedance matrix of polygon, Z_p, at 7GHz from Z_{ER} is

$$Z_p = Q^T Z_{ER} Q = \begin{bmatrix} Z_{p-xx} & Z_{p-xy} \\ Z_{p-yx} & Z_{p-yy} \end{bmatrix} = \begin{bmatrix} 541.64 & -249 \\ -249 & 541.64 \end{bmatrix} j\Omega \tag{4.9}$$

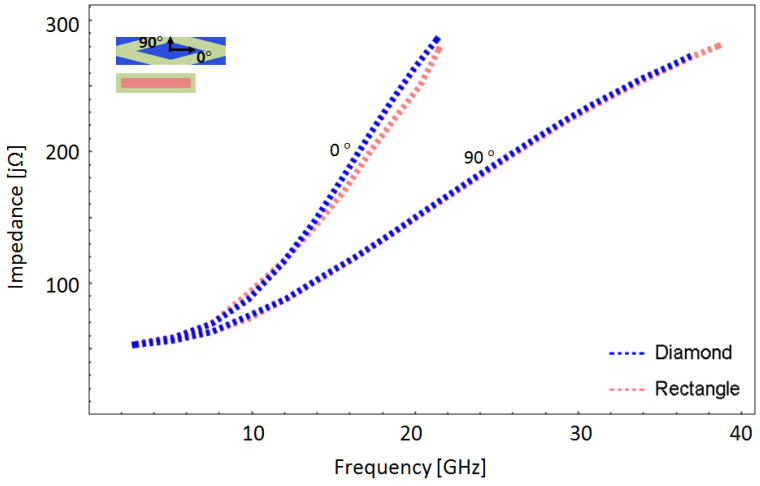

(a)

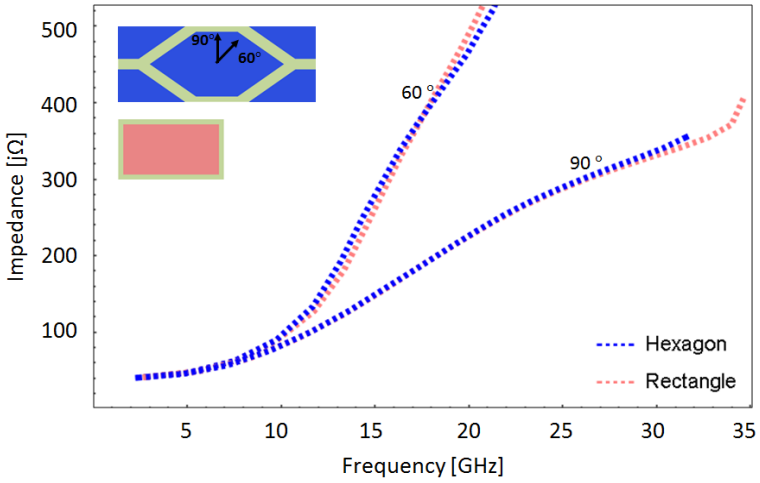

(b)

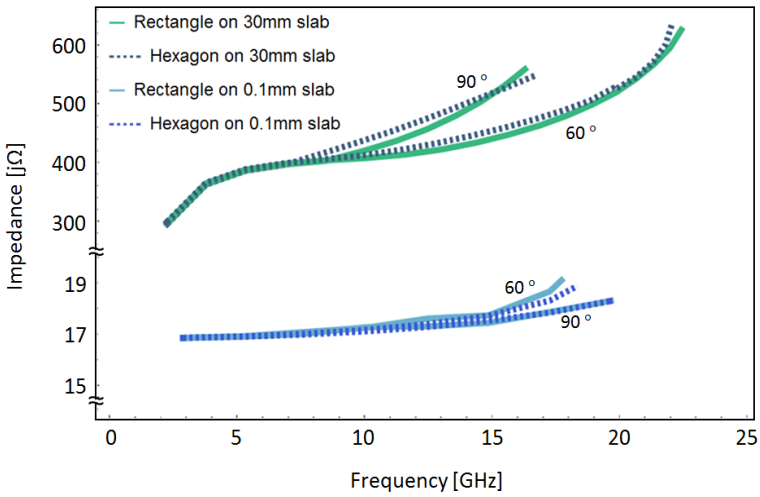

(c)

Figure 4.6: Simulated surface impedance versus frequency for polygon and equivalent rectangle cells

4.3 Unitcell and equivalent rectangle simulation

To prove validity of the equivalent rectangle, we simulated each polygon and equivalent rectangle unit cell in the eigenmode solver. Fig. 4.6 shows frequency-dependent surface impedance plots of polygons and equivalent rectangles. Various propagation directions - 0°, 60° and 90° from the x-axis are simulated (the x-axis is defined as 0°) and those show the impedances of the polygon and the equivalent rectangle are matched well. We note that symmetric polygon cells are taken as examples here to prove this concept since nonsymmetric unit cell cannot be analyzed in the eigenmode solver [17]. In Fig. 4.6 (a) and (b) a thickness of Rogers 5880 grounded slabs is 1.575mm which is in the typical sub-wavelength region. In Fig. 4.6(c) we change the slab thickness of the hexagon and its equivalent rectangle cells to 30mm and 0.1mm thicknesses to verify the technique for the electrically thick and thin slabs. As shown in Fig. 4.6(c), the fair agreements of surface impedances between the hexagon and equivalent rectangle cells are plotted for both cases of 30mm and 0.1mm thickness. The plot of 30mm thickness slab covers from $\frac{\lambda}{4}$ to 2λ frequency range and the plot of 0.1mm thickness slab also show the agreement in $\frac{\lambda}{1000}$ $\frac{\lambda}{166}$ frequncy range.

4.4 Whole pattern and impedance boundary simulation

We also extend this method from a single unit cell to a whole impedance pattern for the purpose of validating our impedance extraction technique. The impedance values extracted from individual unit cells are simulated in tensor impedance boundaries in HFSS, and compared to a simulation of the conducting patches. We start with a simple anisotropic impedance pattern with hexagonal unit cells, which is generated by the point shifting method

[25]. As shown in Fig. 4.7(a), unit cells are symmetric hexagon shapes and form an angle of 45 degrees with $\times$ and y axes. The size of the hexagonal unit cell is 3.58mm in the long dimension and 1.47mm in the short dimension with 0.6mm gaps between the cells, and all cells have same sizes on the pattern. The overall pattern dimensions are 220 $\times$ 220 mm, with 5952 perfectly conducting patches on a grounded 2.5mm thick Rogers 6010 substrate. A coaxial feed is located in the middle of the panel and its diameter is 5mm. Fig. 4.7(b) shows the field plot at 2mm above the board at 5.3GHz from the driven modal solver in Ansys HFSS. The wave propagates faster in low impedance region and move slower in the high impedance direction, so that the anisotropy produces ellipse-shaped patterns of constant phase as expected. The additional variations shown in PEC simulation is indicative of standing wave pattern which is caused by edge scattering.

We calculate the equivalent rectangle and the surface impedance matrix of the hexagonal unit cell using the impedance extraction procedure. The equivalent rectangle of the hexagonal unit cell is 3.4 ellipse 1.45 mm, and the impedance Z_p based on the extracted impedance function is $\begin{bmatrix} 245 & -78 \\ -78 & 245 \end{bmatrix} j\Omega$ at 5.3GHz. For verifying the calculated impedance value Z_p, we have simulated an impedance boundary sheet with the extracted impedance profile. Fig. 4.7(c) shows a part of the impedance boundary sheet which is divided into individual cells which are assigned the effective impedance boundary extracted from the hexagonal unit cells. The impedance Z_p has been applied on each region of the impedance boundary sheet and the size of the whole sheet is the same as the panel that is patterned with conductive cells. In Fig. 4.7(d) we have obtained the field plot that matches with the result of PEC pattern, under the same simulation setup. Except for reflections due to the edges in Fig. 4.7(b), the regions where reflections are not significant still show the same shape of oval with the same aspect ratio.

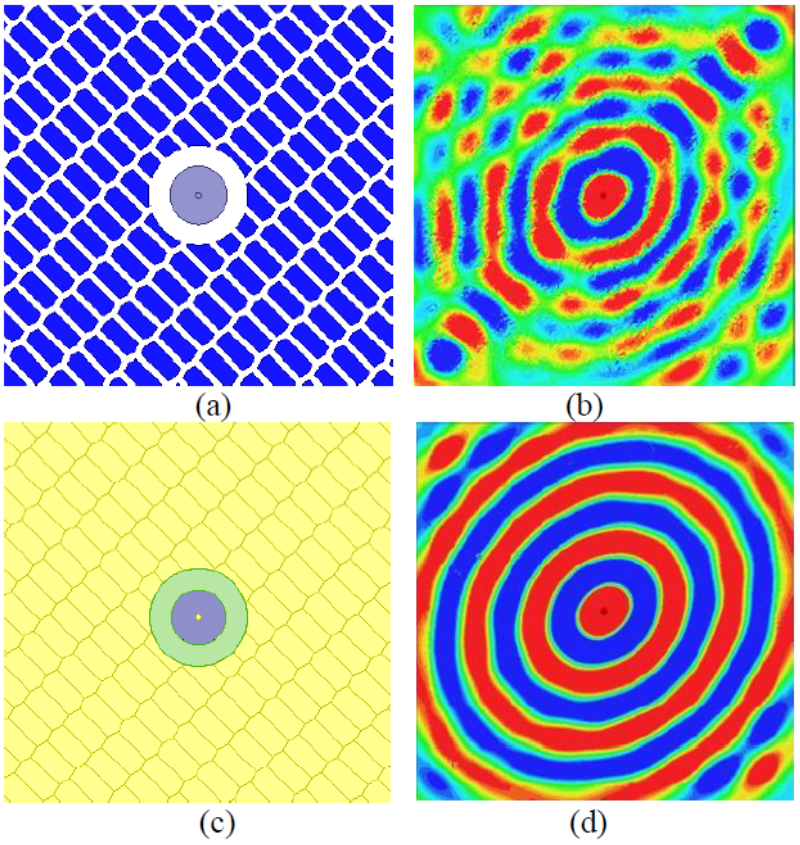

Figure 4.7: Hexagone pattern with PEC pateches and impedance boundary, and field plots (a) Enlarged section of the PEC pattern with hexagon unit cells and a coaxial feed. (b) Normalized electric field at 5.3GHz. (c) Impedance boundaries for extracted tensor impedances of hexagon cells with a coaxial feed. Surface impedance of the substrate, 50jΩ, is applied to the green region. (d) Normalized electric field at 5.3GHz shows same field trend with the PEC pattern.

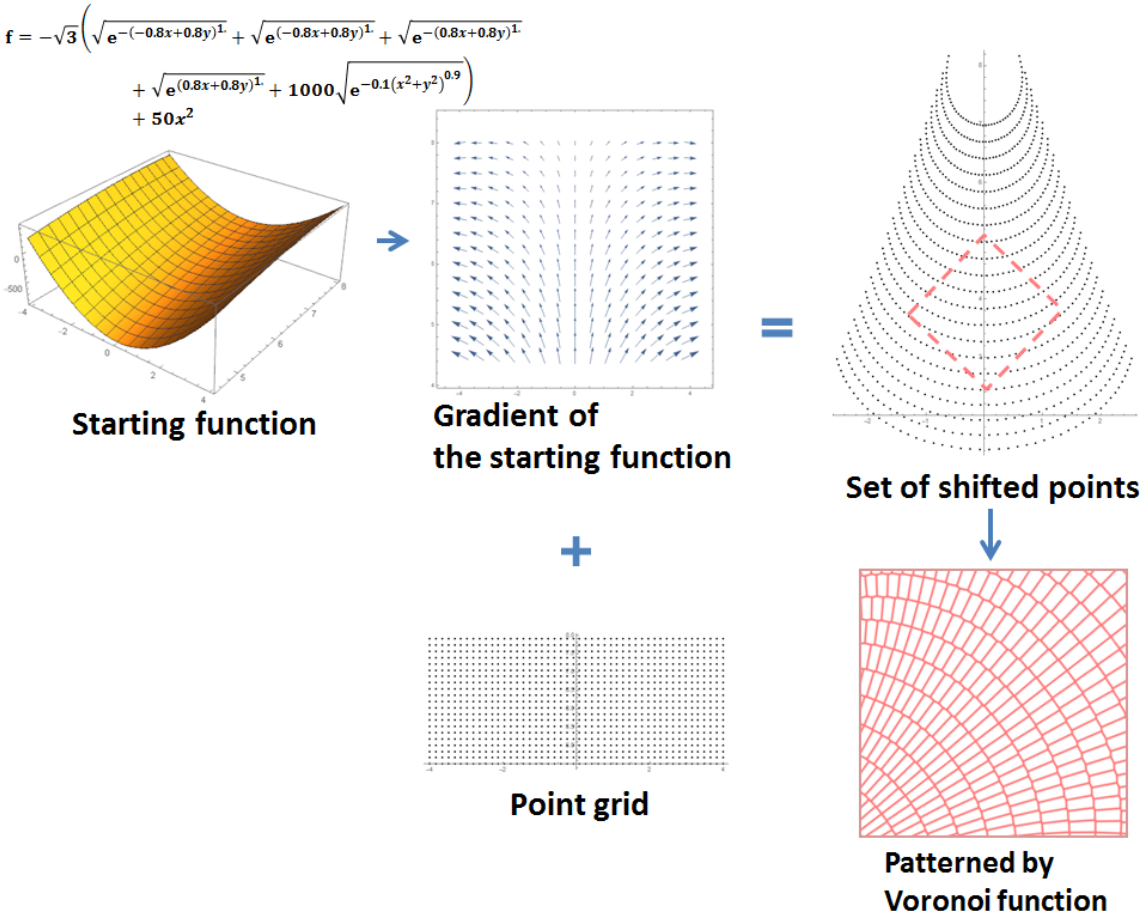

Figure 4.8: Procedure of designing a 90 degree beam shifter

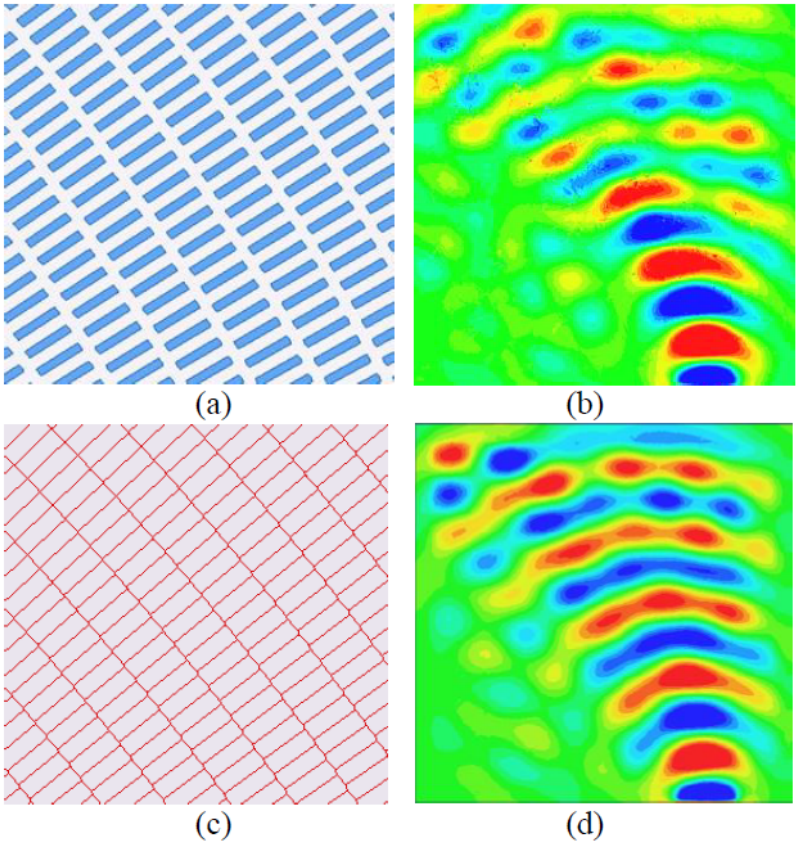

Figure 4.9: 90 degree beam shifter pattern with PEC pateches and impedance boundary, and field plots (a) A part of the PEC pattern with anisotropic polygon cells. (b) Normalized electric field at 7GHz. (c) Impedance boundaries for extracted tensor impedances of polygon cells. (d) Normalized electric field at 7GHz shows same field trend with the PEC pattern.

We generated an additional surface impedance pattern using the point shifting method, which is highly anisotropic, and smoothly varies the direction of high impedance over a 90 degree rotation. A part of the pattern is shown in Fig. 4.9(a).

Each elongated polygon unit cell which is close to a rectangular cell has slightly different shape and size as the pattern has a gradual change with the rotation angle. It has different orientations of maximum and minimum values of impedance so that every cell has a different surface impedance Z_p tensor. The overall pattern dimensions are 150 $\times$ 150 mm, with 7750 conductive patches on a grounded 2.5mm thick Rogers 6010 substrate, and

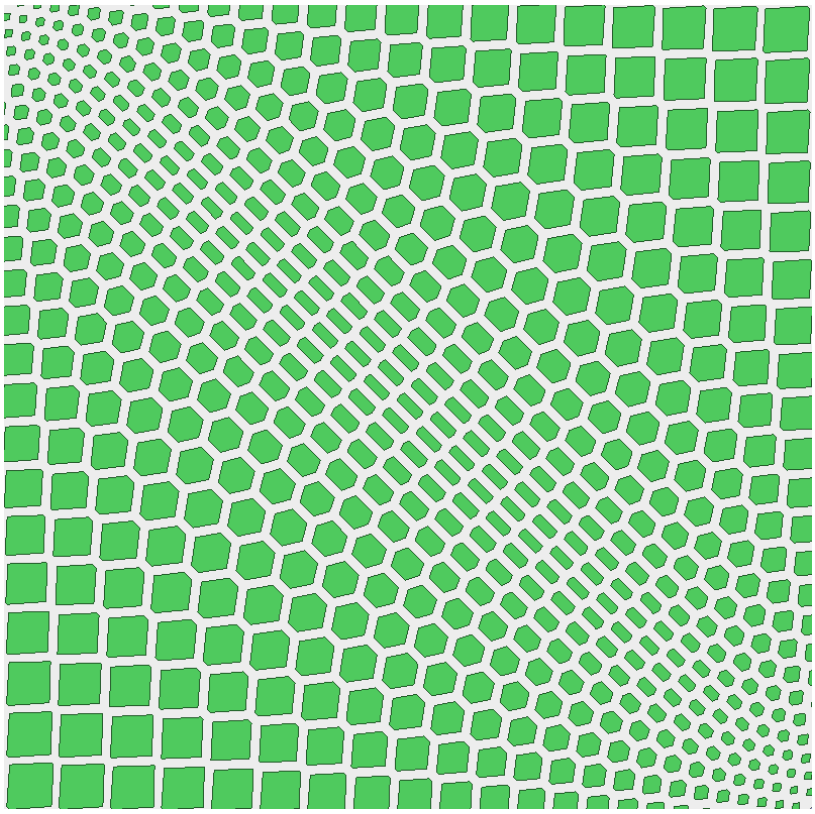

Figure 4.10: Enlarged section of the PEC pattern. The largest cell size is 3 $\times$ 3 mm and the smallest one is 0.5 $\times$ 0.5mm. The gaps between patches are 0.6mm.

there are 0.6mm gaps between the cells. A thin, wide rectangular source is placed at the right bottom edge of the panel for excitation. Fig. 4.9(b) shows the field plot of the whole panel at 2mm above the board at 7GHz analyzed in the driven modal solver in HFSS. The sets of Z_p from the impedance extraction method are applied to each impedance boundary region correspondingly which is shown in Fig. 4.9(c). As elongated unit cells have a smooth transition towards 90 degrees, the range of Z_{p-xx} is 468.23 j to 236.65 jΩ and Z_{p-yy} is 231.86 jΩ to 464.28 jΩ at 7GHz. Fig. 4.9(d) shows the field plot from the impedance boundary simulation which has the same trend as the panel consisting of conducting patches, verifying that the impedances extracted from the metallic patches are accurate.

Fig. 8 shows another inhomogeneous pattern including smoothly varying impedance

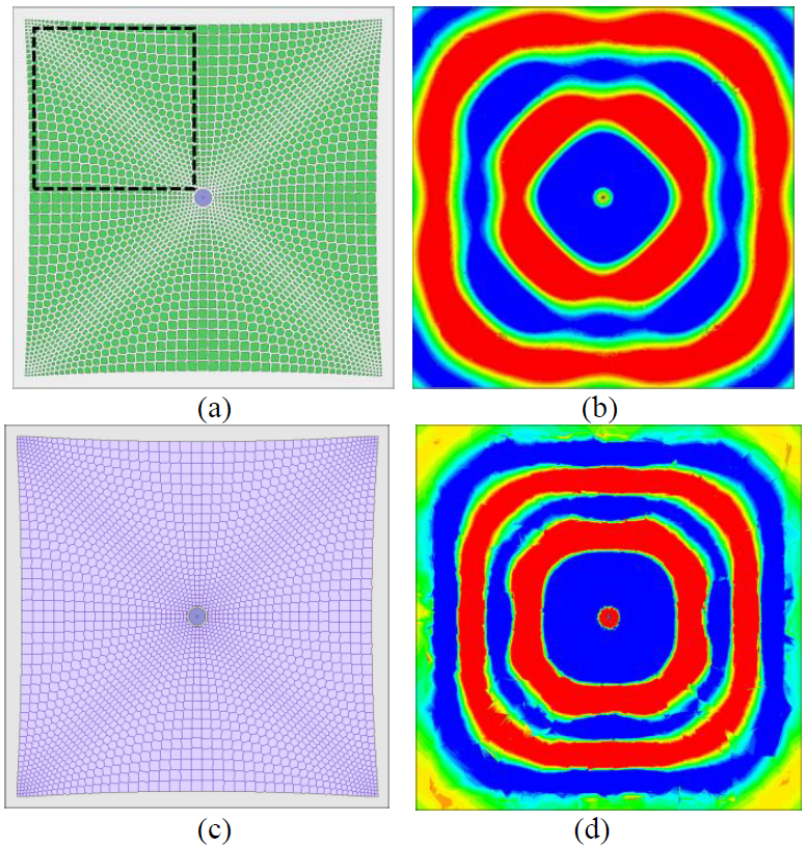

Figure 4.11: Square field pattern with PEC pateches and impedance boundary, and field plots. (a) Pattern on the board with a coaxial feed. (b) Normalized electric field at 9GHz at 2mm above the PEC pattern. Circular fields from the coaxial feed turn into square fields as it follows the impedance surface. (c) Impedance boundaries corresponding to polygon unit cells and the board. (d) Normalized electric field at 9GHz at 2mm above the impedance boundary plane.

transition with various shapes of unit cells. As shown in Fig. 4.11(a), the pattern consists of both isotropic and anisotropic cells which have different shapes and sizes. Fig. 4.11(b) is a whole PEC pattern on 1.5mm thick Rogers 6010 and the same coaxcial feed from Fig. 4.7 is located in the middle of the plane. The board dimensions are 110 $\times$ 110 mm with the pattern consisting of 2580 perfectly conducting patches. Fig. 4.11(c) shows a normalized field plot at 2mm above the PEC pattern at 9GHz.The range of Z_{p-xx} is 480.128 jΩ to 98.58 jΩ and Z_{p-yy} is 480.13 jΩ to 98.58 jΩ at 9GHz. In Fig. 4.11(c) the field at the four corners propagates fater since the impedances in diagonal directions are lower than neighboring impedances as the transition of unit cells shows in the pattern. These stretched fields in the diagonal directions make planar wavefronts in the four directions which could be useful to feed a planewave in multiple directions. Fig. 4.11(e) is a normalized field plot at 9GHz from the impedance boundary simulation with the extracted tensor impedance set. The agremment between two simulations proves that the technique extracts tensor impedances within a reliable margin of error.

4.5 Near field scanning measurement

The hexagonal cell pattern was fabricated using printed circuit fabrication technology, and is shown in Fig. 4.12(a). The panel is 230 $\times$ 230 mm with 5952 copper patches on top of the board, and bottom of the board is a ground plane. There is a 5mm diameter hole in the middle of the pattern for a coaxial feed which is the excitation source. A vertical probe was swept 2mm above the surface along a 1mm grid and an Agilent E5071C vector network analyzer recorded the magnitude and the phase of the surface wave. Normalized field results are shown in Fig. 4.12(b). The circular wavefronts generated by the feed are transformed into elliptical wavefronts as they follow the anisotropic impedance profile, as expected. The

result is matched with Fig. 4.7(b) including the effect shown by edge scattering.

The 90 degrees curve pattern and its measurement setup are shown in Fig. 4.12(c). The feed is a trapezoidal sheet of Rogers 5880 and an end-launch SMA adapter is attached to the back of the feed, which functions as a small H-plane sectoral horn. A field map was produced in the same way as with the hexagonal cell pattern described above, and is plotted in Fig. 4.12(d). The 35mm wide flat wavefronts excited by the feed smoothly move from the bottom edge to the left side edge of the panel along the anisotropic impedance pattern of the structure.

4.6 Impedance matching by smoothly varying anisotropic impedance surface patterns

4.6.1 Overview

We apply the 90 degree beam shifter pattern in Fig. 4.8 to impedance matching between two circuits as shown in Fig. 4.13. The modified 90 degree curve pattern is designed to yield the requested resistance and capacitance values in the specified orientation including a transition area that will properly match the two circuits together.

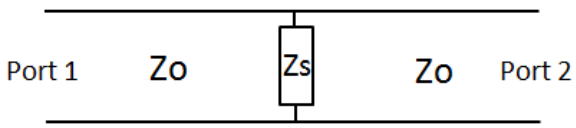

$$\Gamma = \frac{(Z_s || Z_o) - Z_o}{(Z_s || Z_o) + Z_o}$$

$$Z_o = 377 * (\frac{length}{width})$$

Figure 4.16: Circuit topology of the unit cell simulation

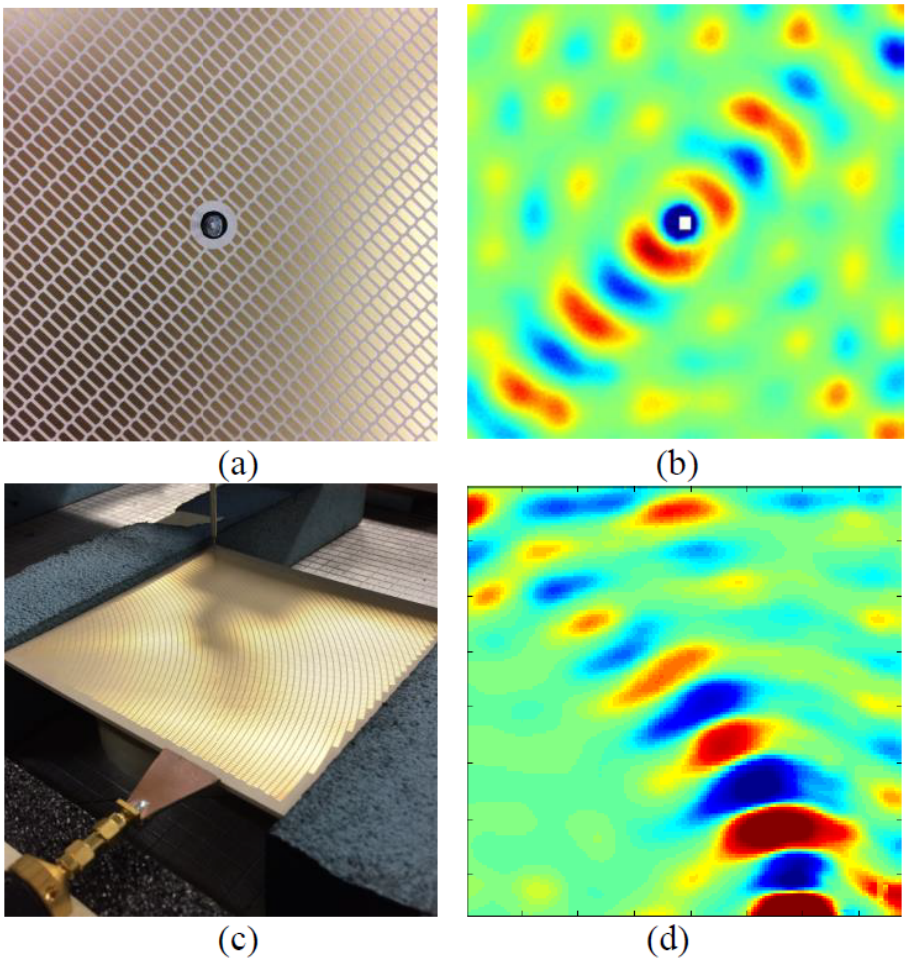

Figure 4.12: Measurement results of hexagone pattern and 90 degree beam shifter. (a) Close-up photo of the fabricated hexagon cells pattern. (b) Normalized near field plot of the surface waves scanned over a 230 $\times$ 230 mm area. (c) Details of the feed and the measurement technique for the fabricated 90degrees curved pattern (d) Normalized near field plot of the surface waves scanned over a 150 $\times$ 150mm area.

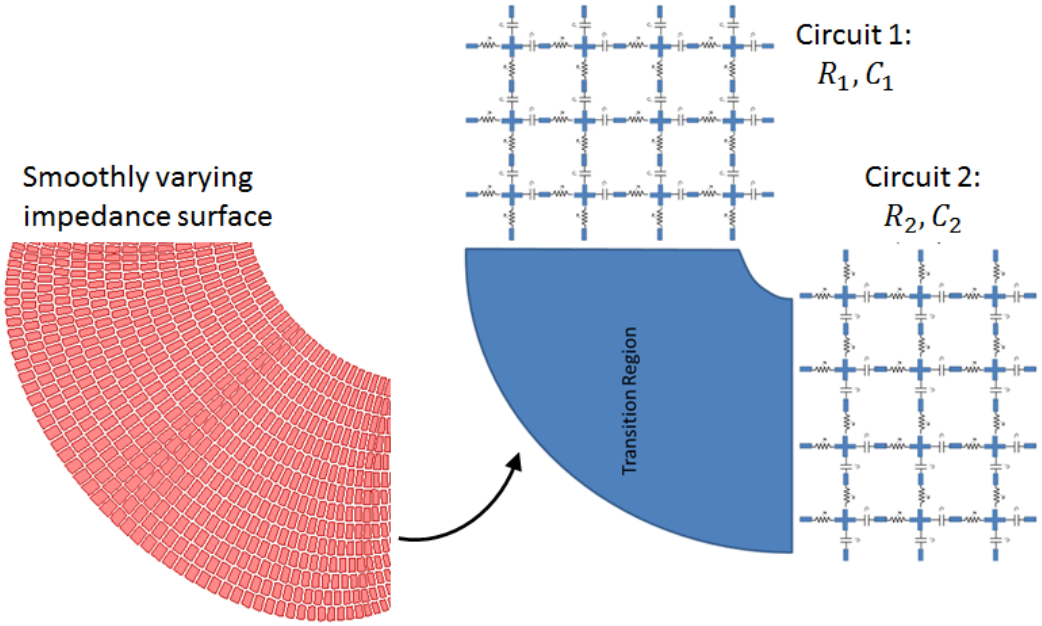

Figure 4.13: Transitioning Two Circuits. Using a smoothly varying 90 degree curve pattern for transitioning between two circuits

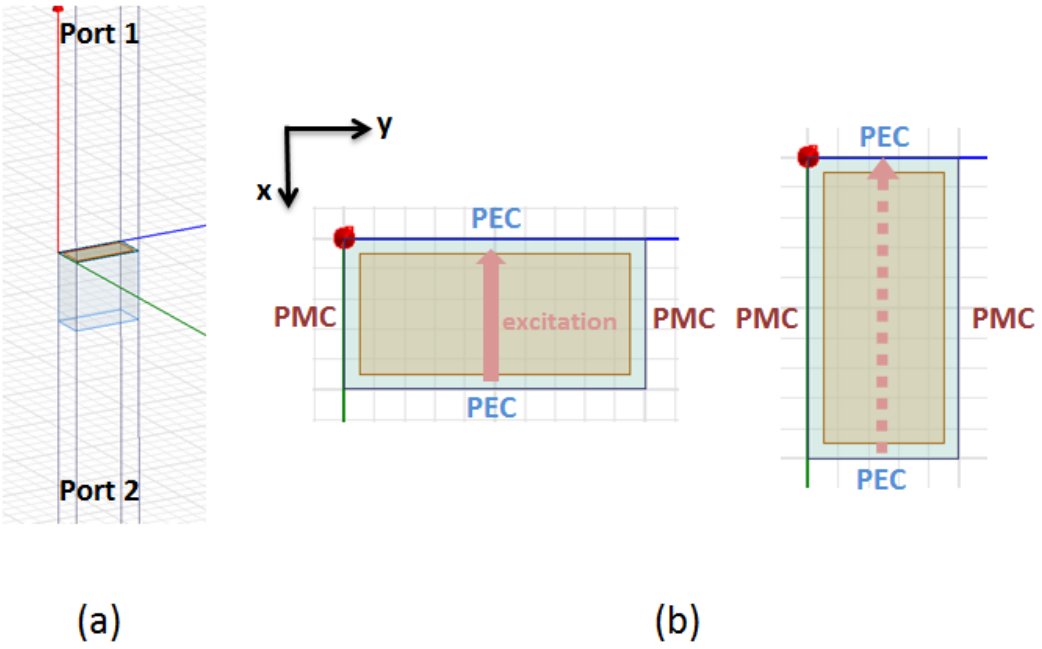

Figure 4.14: Simulation set up and a unit cell structure (a) A unit cell structure with boundaries. (b) Top view of the unit cells.

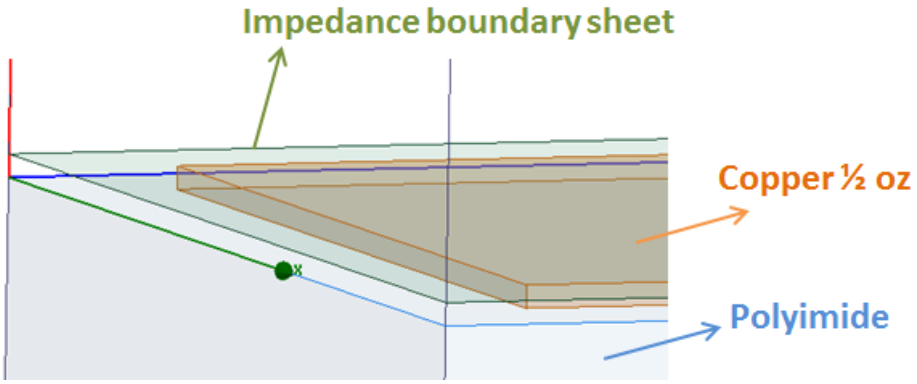

Figure 4.15: Materials of the unit cell structure

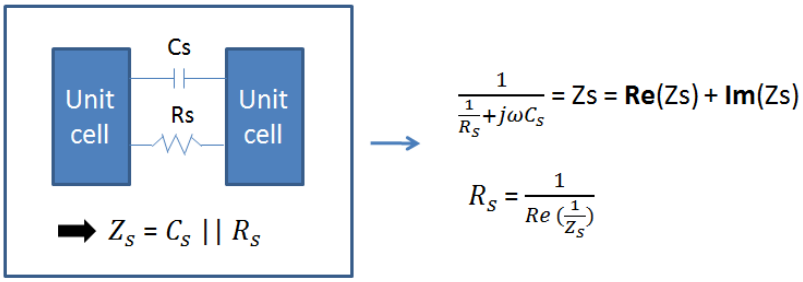

Figure 4.17: Resistance and reactance of the surface shown in a diagram and equations

4.6.2 Unit cell simulation

Fig. 4.14 shows simulation set up and a unit cell structure. The unit cell has been simulated in the driven solver in HFSS with PEC and PMC boundaries. As shown in Fig. 4.14(a) the structure is located in the middle between port 1 and 2. The unit cell with a solid integration line in Fig. 4.14(b) varies its transverse length from 1mm to 5mm while its vertical length is 1mm. The other unit cell with a dashed integration line in Fig. 4.14(b) varies its vertical length from 1mm to 5mm while its transverse length is 1mm. The gaps between patches are 0.7mm.

Fig. 4.15 shows an enlarged part of the unit cell. The 0.5 oz copper patch sits on the

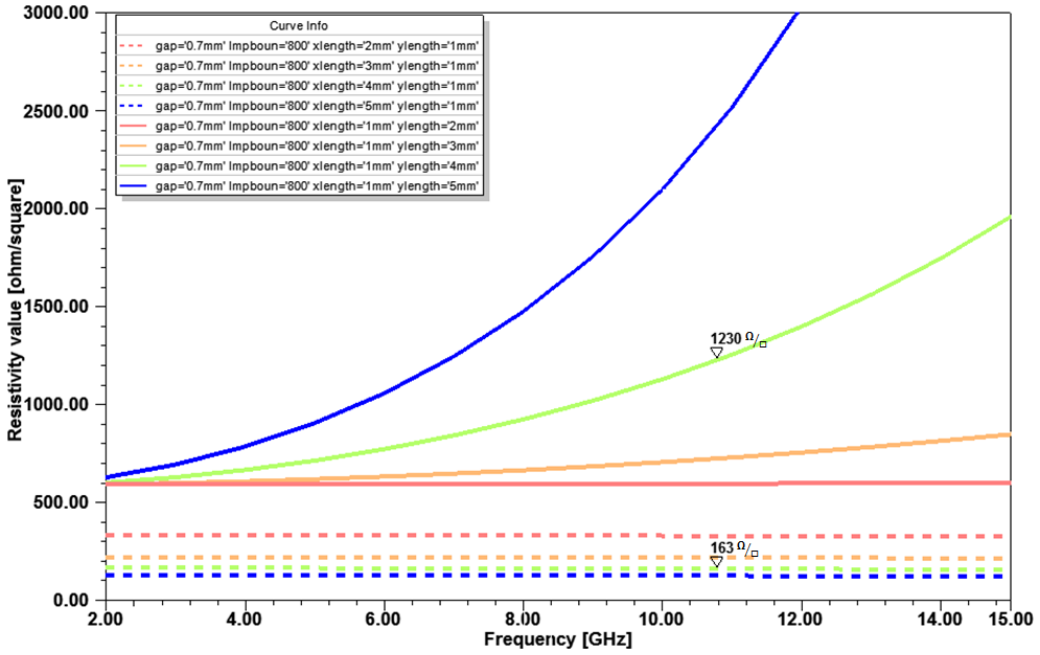

(a)

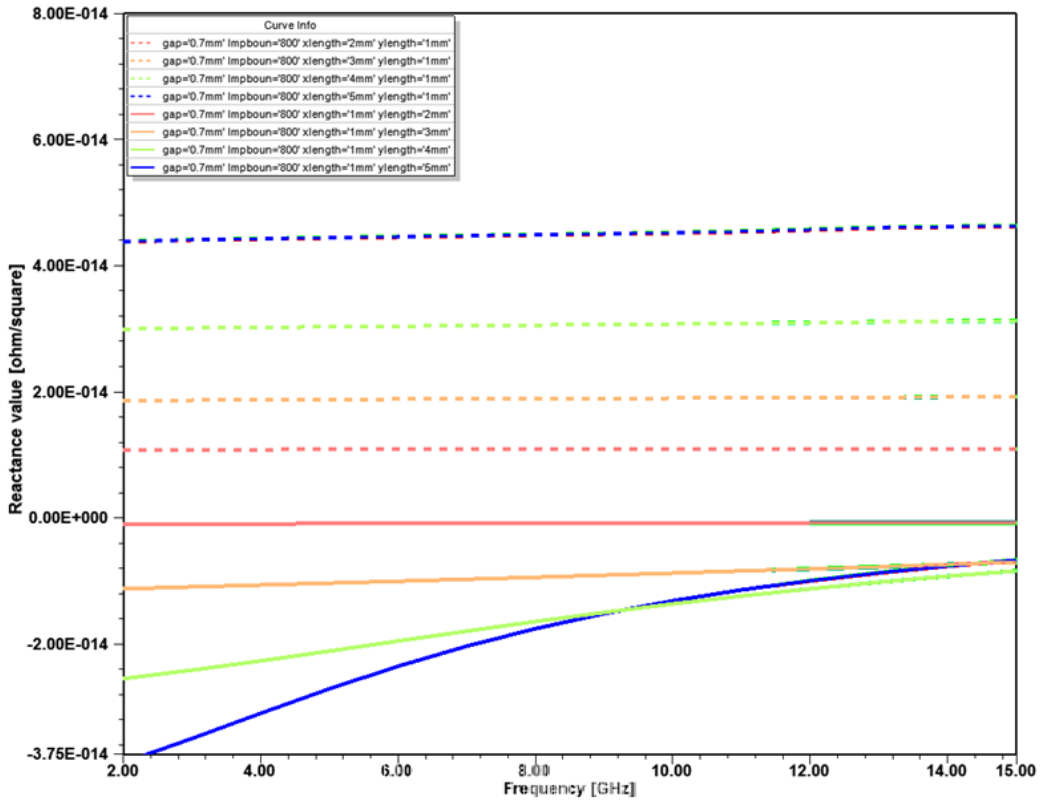

(b)

Figure 4.18: Simulated surface impedance versus frequency for the upright rectangle cell (dashed lines) and the horizontally elongated rectangle cell

polyimide substrate and the 800 $\frac{\Omega}{\square}$ impedance boundary sheet is top of the copper patch.The thickness of polyimide substrate is 0.025mm.

Fig. 4.16 is a circuit topology of the simulation structure for Fig. 4.14(a). We obtain reflection coefficient γ from the simulation and calculate the impedance Z_s. Fig. 4.17 presents resistance and reactance of the surface shown in a diagram and equations. Fig. 4.18 shows resistance and reactance values versus frequency. In Fig. 4.18(a) the resistivity values are not influenced much by the transverse dimension at lower frequency, below 3GHz, and they change dramatically after 4GHz when the transverse dimension varies. As shown in Fig. 4.18(b) reactance values show opposite trend that the reactance doesn't change much as the frequency goes higher.

4.7 Conclusion

We have introduced an approach to extract surface impedances of polygon unit cells using the second moment of inertia equations. This method has an ability to calculate the impedance for nonsymmetric patch cells, which cannot be obtained directly from eigenmode simulations.

This approach has been developed based on the idea that a propagation dimension of unit cell affects its surface tensor impedances. This method which is using momentum of inertia could be useful and applicable to other metamaterials in certain way if properties of their structures or unit cells are related with dimensions. In this paper we limit our method only in the metal patch case.

We have demonstrated that the extracted impedances obtained from the equivalent rectangle are matched with the impedances of the original polygon unit cells. We have chosen a simple and practical example to validate our method experimentally, in the form

of a hexagonal anisotropic pattern as well as an anisotropic 90 degree curved pattern and a square field pattern.

We also have used the 90 degree curved pattern for impedance matching transition area between two circuits. The unit cell simulation results are shown, which include resistance and reactance values of the surface versus frequency.

Chapter 4 is based on and is mostly a reprint of the following paper: **J. Lee**, D. Sievenpiper, Extracting Surface Impedance Method for an Anisotropic Polygon Unit Cell,*IEEE Antennas and Propagation Symposium*, San Diego, CA, July 9, 2017; **J. Lee**, D. Sievenpiper, "Method for Extracting the Effective Tensor Surface Impedance Function from Nonuniform, Anisotropic, Conductive Patterns", *IEEE Transactions on Antennas and Propagation*, Submitted. The dissertation author was the primary author of this material.

Chapter 5

Tensor Impedance Matrix and Starting Function

5.1 Motivation

In chapter 2, we have discussed the patterning technique which is called the point shifting method. In this method the impedance surfaces are designed by a starting function that is related to the desired surface impedance in each direction, which is related to the cell size in that direction. We have chosen this starting function based on knowledge of the desired cell profile.

However, the starting function is related with the desired surface impedances but the function itself is not the tensor impedance function. From the procedure of designing impedance surfaces shown in Fig. 1.6, our goal is to generate a impedance pattern based on the desired surface tensor impedances. In this chapter we investigate the relationship between tensor impedances and starting functions so that we can extend the scope of the point shifting method. We also present a overview of vector integral calculus and integral

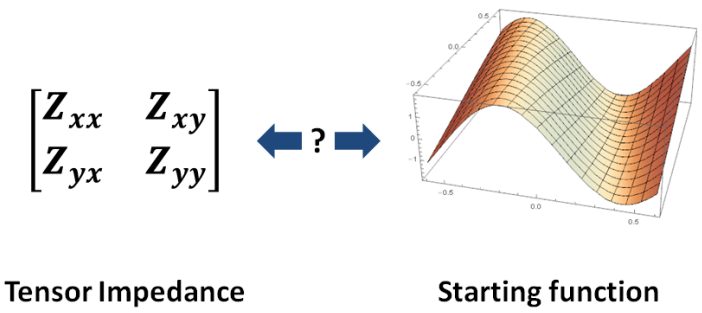

Figure 5.1: Tensor impedance and starting function. A starting function is related to surface impedances but it is not a tensor impedance function itself.

theorems which are used for building a connection between tensor matrix and the starting functions.

5.2 Vector integral of tensor matrix

5.2.1 Intergral theorems

$$\boldsymbol{F} = F(x,y) \underset{\nabla^{-1}}{\overset{\nabla}{\rightleftarrows}} \nabla \boldsymbol{F} = \left[\frac{\partial F(x,y)}{\partial x}, \frac{\partial F(x,y)}{\partial y}\right] \underset{\nabla^{-1}}{\overset{\nabla}{\rightleftarrows}} \nabla(\nabla \boldsymbol{F}) = \begin{bmatrix} \frac{\partial^2 F(x,y)}{\partial x^2} & \frac{\partial^2 F(x,y)}{\partial x \partial y} \\ \frac{\partial^2 F(x,y)}{\partial y \partial x} & \frac{\partial^2 F(x,y)}{\partial y^2} \end{bmatrix}$$

Starting function | Vector function | Tensor matrix of the starting function

Figure 5.2: Definition of starting function, vector function and tensor matrix of the starting function and their relationship

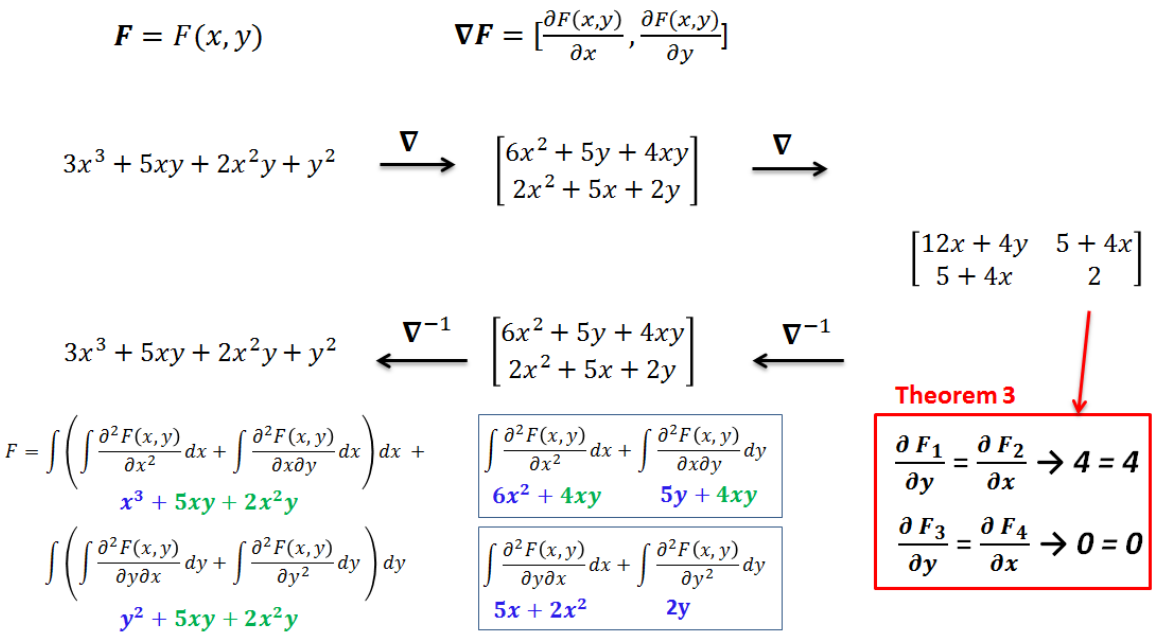

Figure 5.3: Example of gradient and inverse gradient procedure. The vectors in the tensor matrix meet the condition for path independent.

As shown in Fig. 5.2 the gradient of the starting function is a vector function and the gradient of the vector function is a tensor matrix. The tensor matrix from the starting function is brought since we assume that it may have a relationship with a surface tensor impedance matrix. This assumption is based on the property of patch style unit cells that the surface tensor impedances depend on a dimension of unit cell in the propagation direction. Here we call double vector integrals of the tensor matrix as 'inverse gradient process'. To take the vector integral of the tensor matrix in order to have the starting function, the integral should be path independent in a domain D in space. When there is line intergral

$$\int_C \mathbf{F} \cdot d\mathbf{r} = \int_C (F_1 dx + F_2 dy + F_3 dx) \qquad (d\mathbf{r} = [dx, dy, dz]) \tag{5.1}$$

and we see that path independence of the integral in a domain D holds if and only if:

(*Theorem*1) **F** = grad f, where grad f is the gradient of f

(*Theorem*2) Integration around closed curves C in D always gives 0.

(*Theorem*3) curl**F=0**, provided D is simply connected.

We focus on the theorem 3, which is practical to set the tensor matrix for the starting function. From the theorem 3, components should meet the following condition below

$$\frac{\partial F_3}{\partial y} = \frac{\partial F_2}{\partial z}, \qquad \frac{\partial F_1}{\partial z} = \frac{\partial F_3}{\partial x}, \qquad \frac{\partial F_2}{\partial x} = \frac{\partial F_1}{\partial y} \tag{5.2}$$

5.2.2 Vector integral of tensor matrix and starting function

Fig. 5.3 is an example of vector integral of tensor matrix. The tensor matrix meets the condition of path independence. Fig. 5.4 is another example that the starting function includes the first order and constant terms. It shows the first order term and constant terms are not restored at the starting function (b) which is calculated from the tensor matrix. For checking reliability of the inverse gradient process we generate patterns using the point shifting method with starting function (a) and (b) from Fig. 5.4.

Fig. 5.5 shows sets of shifted points and patterns designed by starting function (a) and (b). The set black dots are point grids and the set of pink dots are the shifted points by the gradient of the starting function. Since the first order terms of the starting function become constant terms in the vector function after taking gradient, it only affects on position of dots, not on the design of pattern.

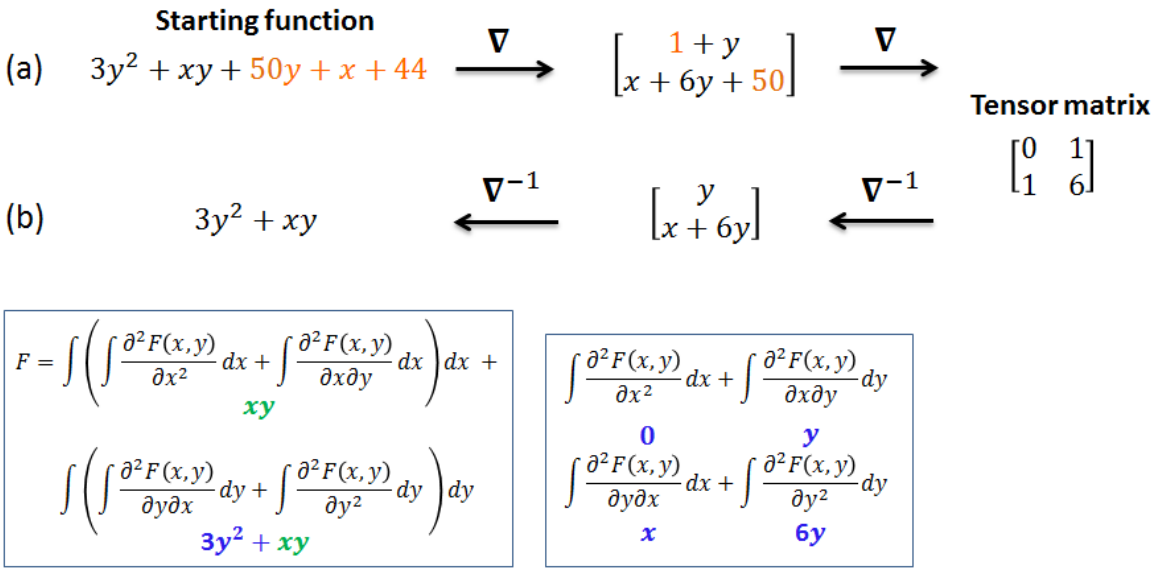

Figure 5.4: Example of gradient and inverse gradient procedure with the first order and constant terms. The inverse gradient of the tensor matrix can not restore the first order and constant terms of the original starting function.

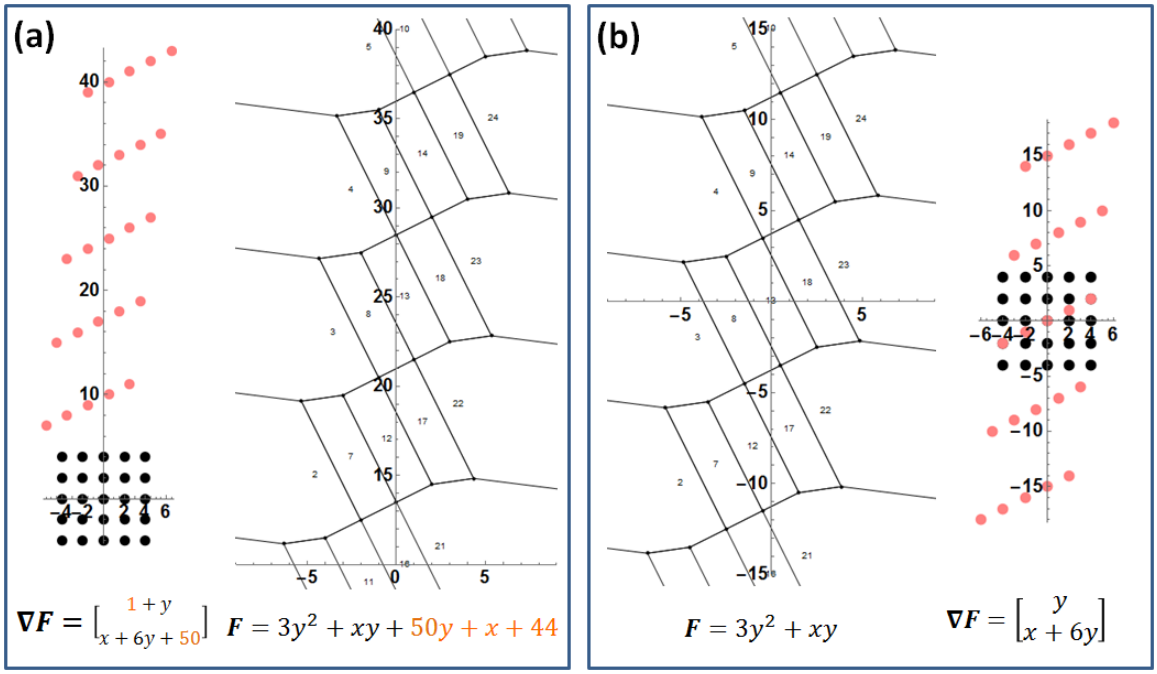

Figure 5.5: Patterns by the original starting function and the developed starting function from tensor matrix. (a)The original starting function and its pattern. (b) The starting function calculated from tensor matrix and its pattern. The patterns are not changed by the first order and constant term. Those terms only affect on the position of the pattern.

5.3 Conclusion

This chapter has studied the relationship between tensor matrix and starting functions, and addressed the inverse gradient process by vector integral calculation. The vectors of the tensor matrix must be path independent in the inverse gradient process. We have calculated couple of inverse gradient processes and showed validity of patterns which are generated from tensor matrix. A further study on correlation between the tensor matrix and surface tensor impedance would be useful in designing impedance surfaces based on the desired tensor impedance function.

Chapter 6

Conclusion

6.1 Summary of Work

This dissertation presents patterning and a validation methods for arbitrary anisotropic impedance surfaces and introduces practical applications generated by the point shifting method.

Chapter 2 discussed a new patterning technique, the point-shifting method which allows us to generate smoothly varying arbitrary anisotropic impedance surfaces. A 2D Luneburg lens and a beam shifter have been simulated and measured.

Chapter 3 demonstrate a pattern that can be used for shielding two dimensional area from surface waves. Several designs for surface waves shielding are studied and shown that high surface impedance resign can block the surface waves from an object placed on a surface.

Chapter 4 addresses a validation technique to extract the effective tensor surface impedance function from nonuniform, anisotropic, conductive Patterns. The method enable to find tensor surface impedances for asymmetric and polygon unit cells which are not

possible to be analyzed in periodic boundaries.

Chapter 5 studies a relationship between a starting function and tensor impedance function. As the tensor impedance function meeting the condition of inverse gradient is found, we can design a pattern based on the tensor impedance in a certain condition.

6.2 Future work

The work has covered most of procedure of designing arbitrary anisotropic impedance surface based on desired tensor impedances as shown in Fig. 1.6. Current patterning technique designs impedance surfaces based on the starting function. As mentioned in chapter 5, if the relationship between tensor matrix of the starting function and desired tensor impedance functions is found, it would allow us to more easily pattern the desired impedance surfaces and complete the design process.

In this thesis, we have discussed the patch style unit cells and surface impedance patterns, which support TM mode. Since unit cells generated by the point shifting method have variety of shapes, and often asymmetric unit cells will support TM, TE, or mixed TM/TE modes depending on the direction of propagation, it would be useful to explore TE or mixed mode characteristic in arbitrary anisotropic patterns. Also this patterning technique could be used with via or active components, or would be developed and applicable to design a pattern for 3D structure.

Bibliography

[1] R. G. Quarfoth and D. F. Sievenpiper. Nonscattering waveguides based on tensor impedance surfaces. *Antennas and Propagation, IEEE Transactions on*, 63(4):1746–1755, 2015.

[2] A. M. Patel and A. Grbic. Transformation electromagnetics devices based on printed-circuit tensor impedance surfaces. *Microwave Theory and Techniques, IEEE Transactions on*, 62(5):1102–1111, 2014.

[3] R. Quarfoth and D. Sievenpiper. Surface wave scattering reduction using beam shifters. *Antennas and Wireless Propagation Letters, IEEE*, 13:963–966, 2014.

[4] Dan Sievenpiper, J. Colburn, B. Fong, J. Ottusch, and J. Visher. Holographic artificial impedance surfaces for conformal antennas. In *Antennas and Propagation Society International Symposium, 2005 IEEE*, volume 1B, pages 256–259 vol. 1B.

[5] R. Quarfoth and D. Sievenpiper. Artificial tensor impedance surface waveguides. *Antennas and Propagation, IEEE Transactions on*, 61(7):3597–3606, 2013.

[6] C. L. Holloway, E. F. Kuester, J. A. Gordon, J. O' Hara, J. Booth, and D. R. Smith. An overview of the theory and applications of metasurfaces: The two-dimensional equivalents of metamaterials. *IEEE Antennas and Propagation Magazine*, 54(2):10–35, 2012.

[7] C. L. Holloway, D. C. Love, E. F. Kuester, J. A. Gordon, and D. A. Hill. Use of generalized sheet transition conditions to model guided waves on metasurfaces/metafilms. *IEEE Transactions on Antennas and Propagation*, 60(11):5173–5186, 2012.

[8] Dan Sievenpiper, Zhang Lijun, R. F. J. Broas, N. G. Alexopolous, and E. Yablonovitch. High-impedance electromagnetic surfaces with a forbidden frequency band. *Microwave Theory and Techniques, IEEE Transactions on*, 47(11):2059–2074, 1999.

[9] B. H. Fong, J. S. Colburn, J. J. Ottusch, J. L. Visher, and D. F. Sievenpiper. Scalar and tensor holographic artificial impedance surfaces. *Antennas and Propagation, IEEE Transactions on*, 58(10):3212–3221, 2010.

[10] G. Minatti, M. Faenzi, E. Martini, F. Caminita, P. De Vita, Gonza, x, D. lez Ovejero, M. Sabbadini, and S. Maci. Modulated metasurface antennas for space: Synthesis, analysis and realizations. *Antennas and Propagation, IEEE Transactions on*, 63(4):1288–1300, 2015.

[11] C. Pfeiffer and A. Grbic. Planar lens antennas of subwavelength thickness: Collimating leaky-waves with metasurfaces. *Antennas and Propagation, IEEE Transactions on*, 63(7):3248–3253, 2015.

[12] Lars Valerian Ahlfors. *Conformal invariants: topics in geometric function theory*, volume 371. American Mathematical Soc., 2010.

[13] Ulf Leonhardt. Optical conformal mapping. *Science*, 312(5781):1777–1780, 2006.

[14] Huanyang Chen, C. T. Chan, and Ping Sheng. Transformation optics and metamaterials. *Nat Mater*, 9(5):387–396, 2010.

[15] S. H. Lo. A new mesh generation scheme for arbitrary planar domains. *International Journal for Numerical Methods in Engineering*, 21(8):1403–1426, 1985.

[16] Mark De Berg, Marc Van Kreveld, Mark Overmars, and Otfried Cheong Schwarzkopf. *Computational geometry*. Springer, 2000.

[17] Lon Brillouin. *Wave propagation in periodic structures: electric filters and crystal lattices*. Courier Corporation, 2003.

[18] C. Pfeiffer and A. Grbic. A printed, broadband luneburg lens antenna. *Antennas and Propagation, IEEE Transactions on*, 58(9):3055–3059, 2010.

[19] Kenichi Sato and Hiroshi Ujiie. A plate luneberg lens with the permittivity distribution controlled by hole density. *Electronics and Communications in Japan (Part I: Communications)*, 85(9):1–12, 2002.

[20] R. Quarfoth and D. Sievenpiper. Anisotropic surface impedance cloak. In *Antennas and Propagation Society International Symposium (APSURSI), 2012 IEEE*, pages 1–2.

[21] R. Quarfoth and D. Sievenpiper. Broadband unit-cell design for highly anisotropic impedance surfaces. *Antennas and Propagation, IEEE Transactions on*, 62(8):4143–4152, 2014.

[22] Robert E. Collin. *Field theory of guided waves*. Wiley-IEEE Press, 1991.

[23] Huang Ming, Yang Shiwen, Gao Fei, R. Quarfoth, and D. Sievenpiper. A 2-d multibeam half maxwell fish-eye lens antenna using high impedance surfaces. *Antennas and Wireless Propagation Letters, IEEE*, 13:365–368, 2014.

[24] D. J. Gregoire and A. V. Kabakian. Surface-wave waveguides. *IEEE Antennas and Wireless Propagation Letters*, 10:1512–1515, 2011.

[25] J. Lee and D. F. Sievenpiper. Patterning technique for generating arbitrary anisotropic impedance surfaces. *IEEE Transactions on Antennas and Propagation*, 64(11):4725–4732, 2016.

[26] R. Quarfoth and D. Sievenpiper. Simulation of anisotropic artificial impedance surface with rectangular and diamond lattices. In *Antennas and Propagation (APSURSI), 2011 IEEE International Symposium on*, pages 1498–1501.

[27] Yun Bo Li, Xiang Wan, Ben Geng Cai, Qiang Cheng, and Tie Jun Cui. Frequency-controls of electromagnetic multi-beam scanning by metasurfaces. *Scientific Reports*, 4:6921, 2014.

[28] Ferdinand P. Beer. *Vector mechanics for engineers.* McGraw-Hill, New York, 2013.

[29] G. Minatti, S. Maci, P. De Vita, A. Freni, and M. Sabbadini. A circularly-polarized isoflux antenna based on anisotropic metasurface. *IEEE Transactions on Antennas and Propagation*, 60(11):4998–5009, 2012.

[30] Gene H Golub and Charles F. Van Loan. *Matrix Computations*. Johns Hopkins University Press, Baltimore, 3rd edition, 1996.